Gondwana Research 54 (2018) 161–179

Contents lists available at ScienceDirect

Gondwana Research

journal homepage: www.elsevier.com/locate/gr

Ore genesis of the Fule Pb—Zn deposit and its relationship with the Emeishan Large Igneous Province: Evidence from mineralogy, bulk C—O—S and in situ S—Pb isotopes

Jia-Xi Zhou [a,c,f,*], Kai Luo [a,b], Xuan-Ce Wang [c], Simon A. Wilde [c], Tao Wu [d,f], Zhi-Long Huang [a], Yin-Liang Cui [e], Jian-Xin Zhao [f]

[a] *Stake Key Laboratory of Ore Deposit Geochemistry, Institute of Geochemistry, Chinese Academy Sciences, Guiyang 550081, China*
[b] *University of Chinese Academy Sciences, Beijing 100049, China*
[c] *The Institute for Geoscience Research, Department of Applied Geology, Curtin University, GPO Box U1987, Perth, WA 6845, Australia*
[d] *School of Earth Sciences, Zhejiang University, Hangzhou 310027, China*
[e] *Yunnan Nonferrous Metals Geological Bureau, Kunming 650051, China*
[f] *Radiogenic Isotope Facility, School of Earth and Environment Sciences, University of Queensland, Brisbane, QLD 4072, Australia*

ARTICLE INFO

Article history:
Received 23 May 2017
Received in revised form 20 October 2017
Accepted 9 November 2017
Available online 10 November 2017

Handling Editor: F. Pirajno

Keywords:
NanoSIMS in situ S isotopes
Fs LA-MC-ICPMS in situ Pb isotopes
Role of Emeishan magmatism
Carbonate-hosted Pb—Zn deposits in the ELIP, South China

ABSTRACT

Magmatic activity plays an important role in mineralization, but little is understood of its role with respect to carbonate-hosted stratabound epigenetic Pb—Zn deposits. The Fule Pb—Zn deposit (~10 Mt of sulfide ore with mean grades of 15–20 wt% Zn + Pb), is stratigraphically placed in middle Permian strata and spatially (~1 m) associated with late Permian continental flood basalts of the Emeishan Large Igneous Province (ELIP). It thus provides an ideal case to investigate its genetic relationship with the ELIP. In addition, the Fule deposit is characterized by high concentrations of Ag, Cd, Ge and Ga, and contains a variety of Cu and Ni sulfide minerals. Syn-ore calcite ($\delta^{13}C = +2.57$–$+3.01$‰) and associated fluids ($\delta^{13}C = +2.96$–$+3.40$‰) have $\delta^{13}C$ values similar to those of fresh limestone ($\delta^{13}C = +1.58$–$+2.63$‰), but the $\delta^{18}O$ values of calcite ($+16.83$–$+19.92$‰) and associated fluids ($+7.80$–$+10.89$‰) are distinctly lower than those of limestone ($\delta^{18}O = +21.85$–$+23.61$‰). This means that C is mainly derived from limestone, whereas the O isotope signature may be related to water/rock (W/R) interaction between mantle and/or metamorphic fluids and limestone. $\delta^{34}S$ values of sulfide minerals obtained by in situ NanoSIMS and conventional bulk techniques record a range of $+9.8$–$+23.1$‰ and $+10.04$–$+16.43$‰, respectively, reflecting the enrichment of heavy S isotopes in the ore-forming fluids and thermochemical sulfate reduction (TSR) is the principal mechanism for the formation of S^{2-}. Cores of sulfide crystals have much higher $\delta^{34}S$ values than their rims, indicating a probable mixture of multiple S reservoirs and/or a dynamic fractionation of S isotopes occurred during sulfide precipitation. The uniform femtosecond (fs) LA-MC-ICPMS in situ Pb isotopic data for galena plot in the field that differs from any of the three potential sources in the region. Such signatures demonstrate that metal Pb was most likely derived from a well-mixed source of basalts, sedimentary rocks and basement rocks. We propose that (a) the enrichment in Ag, Cu, Ni, Cd, Ge and Ga, and the isotope signatures of hydrothermal minerals in the Fule region are related to fluids derived from or flowed through multiple reservoirs; (b) Emeishan magmatism provided heat, elements and associated fluids, and its basalts acted as an impermeable and protective layer; and (c) fluid mixing caused TSR, and then resulted in W/R interaction and CO_2 degassing, all of which played a key role in the precipitation of hydrothermal minerals.

1. Introduction

Carbonate-hosted stratabound epigenetic Pb—Zn deposits, traditionally named as Mississippi Valley-type (MVT), are an important source of base metal ores that form in sediments some time during the lifetime of a sedimentary basin (Anderson and Macqueen, 1982). MVT deposits predominantly form in platform carbonate sequences and are typically located within extensional zones inboard of orogenic belts (Leach et al., 2005). As such type of deposits is characterized by the absence of temporally or spatially associated magmatic activity, the classical thinking about the origin of MVT deposits is that it was related to the low temperature (50–200 °C) and high salinity (10–30 wt% NaCl equiv.) basin brines (Leach et al., 2010). However, many carbonate-hosted Pb—Zn deposits are spatially associated with igneous

---

* Corresponding author at: Stake Key Laboratory of Ore Deposit Geochemistry, Institute of Geochemistry, Chinese Academy Sciences, Guiyang 550081, China.
E-mail address: zhoujiaxi@vip.gyig.ac.cn (J.-X. Zhou).

https://doi.org/10.1016/j.gr.2017.11.004
1342-937X/© 2017 International Association for Gondwana Research. Published by Elsevier B.V. All rights reserved.

rocks, but whether they are related to the igneous activity is unclear and needs to be carefully investigated.

In the western Yangtze Block (Fig. 1a), South China, there are >400 carbonate-hosted Pb—Zn deposits and many basalt-hosted native Cu deposits within the Emeishan Large Igneous Province (ELIP) (Fig. 1b) (Liu and Lin, 1999; Zhu et al., 2007; J.X. Zhou et al., 2014a). These Pb—Zn deposits form the giant Sichuan-Yunnan-Guizhou (SYG) Pb—Zn metallogenic province (Fig. 1a–b), representing ~27% of the total Zn + Pb resources in China, and are an important part of the South China low-temperature metallogenic domain (Zhou et al., 2013a; Wang et al., 2014; Zhang et al., 2015; Hu et al., 2017). The SYG province is structurally bounded by the N-S-trending Anninghe-Lvzhijiang, the NE-SW-trending Mile-Shizong-Shuicheng and the NW-SE-trending Kangding-Yiliang-Shuicheng (Fig. 1a) faults. The Pb—Zn deposits in the SYG province are characterized by (a) ore bodies that are hosted by late Ediacaran to middle Permian carbonate rocks that are spatially associated with late Permian Emeishan continental flood basalts (Figs. 1b, 2–3); (b) ore bodies that have stratiform or lentiform shape within bedding-planes and/or steeply-dipping veins along fault dip planes (Zheng and Wang, 1991; Li et al., 2007; Zhou et al., 2013b; Wei et al., 2015; Jin et al., 2016; Zhu et al., 2016); (c) sulfide ore that has high mean grades of 10–35 wt% Zn + Pb, and high contents of Ag, Cu, Cd, Ge and Ga (Si et al., 2006; Ye et al., 2011; Zhou et al., 2011; J.X. Zhou et al., 2014b; Zhu et al., 2017); and (d) ore-forming fluids of low-medium temperatures (<300 °C) and salinities (<15 wt% NaCl equiv.) (Bai et al., 2013; Li et al., 2015; Zhang et al., 2015; Liu et al., 2017). These features are significantly different from those of typical MVT deposits (Leach et al., 2005, 2010). As the only large-scale igneous event between the Ediacaran and Triassic in the SYG province was eruption of the Emeishan flood basalts, the above mineralization features were generally considered to be related to the ELIP (Huang et al., 2010; Xu et al., 2014; Zhou et al., 2013a, J.X. Zhou et al., 2014a; Li et al., 2016).

The Fule Pb—Zn deposit, hosted by carbonate rocks of the middle Permian Yangxin Formation (Si et al., 2006), is stratigraphically and spatially (~1 m) close to the late Permian Emeishan basalts (Figs. 1b, 2–3). This deposit contains very high ore grades (up to 60 wt% Zn + Pb, mean 15–20 wt%) and is rich in multiple elements (4567 t Cd, 329 t Ge, and 177 t Ga at mean grades of 0.127 wt% Cd, 0.012 wt% Ge, and 0.007 wt% Ga) (Si et al., 2011, 2013; Ye et al., 2011). These features are similar to those of the adjacent world-class Huize Pb—Zn deposit (hosted in Carboniferous strata with >30 Mt of sulfide ore with average grades of 25–35 wt% Zn + Pb) (Fig. 1b) (Zhou et al., 2001; Li et al., 2006; Huang et al., 2010; Bao et al., 2017), which is considered to be a typical representative of the unique SYG-type deposits (related to the ELIP) in the western Yangtze Block (Huang et al., 2010). In spite of this, there is still debate on the ore genesis type, including whether it is a distal magmatic hydrothermal-type (based on geological evidence: Liu and Lin, 1999), stratabound-type (based on trace element data: Si et al., 2006, 2011) or MVT (based on Cd isotopic data: Zhu et al., 2017). Hence, the Fule deposit provides an ideal case for understanding the role of magmatism during the formation of carbonate-hosted Pb—Zn deposits.

Micro-scale variation of elements and isotopes in hydrothermal minerals, obtained by micro-beam analysis, can provide crucial clues for revealing the source and evolution of ore-forming elements and associated fluids, and the cause of hydrothermal mineral precipitation (Barker et al., 2009; Nishizawa et al., 2010; Ye et al., 2011; Jin et al., 2016; Deng et al., 2017). Laser-ablation multi-collector inductively coupled plasma mass spectroscopy (LA-MC-ICPMS) and secondary ion

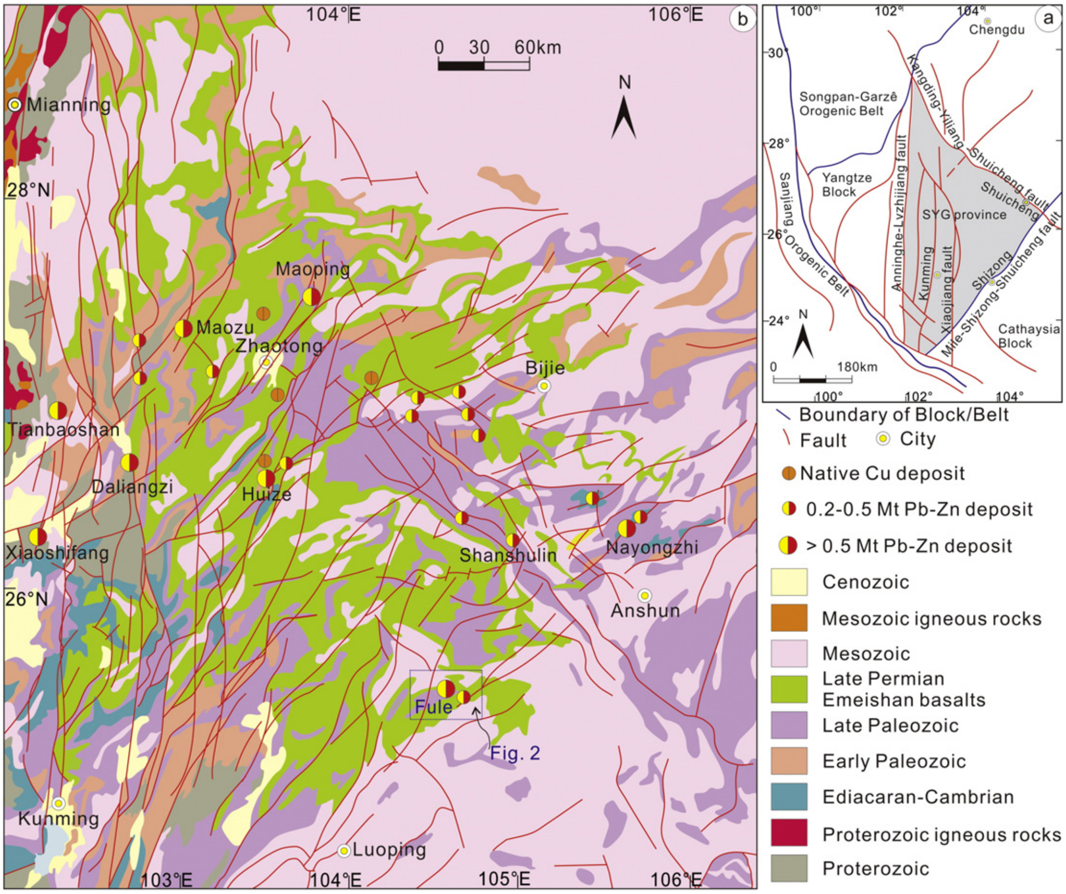

Fig. 1. a: Regional geological setting of SW China, highlighting the general study area; b: Geological sketch map of the Sichuan-Yunnan-Guizhou (SYG) Pb—Zn metallogenic province (modified from Liu and Lin, 1999), which shows the distribution of Pb—Zn deposits, native Cu deposits, strata, faults and igneous rocks.

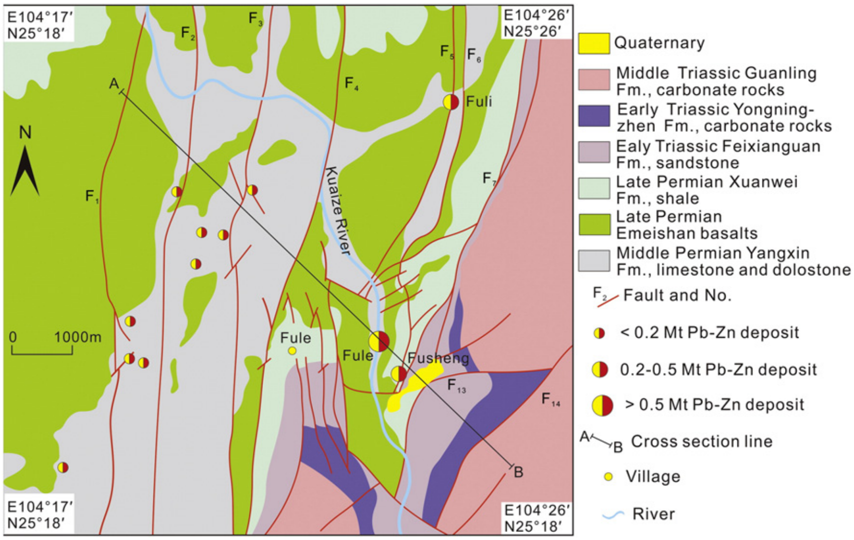

Fig. 2. Geological sketch map of the Fule district (modified from Liu and Lin, 1999), showing the distribution of Pb—Zn deposits, strata, faults and Emeishan basalts.

mass spectroscopy (SIMS) can accurately analyze isotopic compositions of hydrothermal minerals in situ (Ikehata et al., 2008; Zhang et al., 2014; Yuan et al., 2015; Bao et al., 2016). Here we use the Fule deposit as a case study, utilizing NanoSIMS in situ S, femtosecond (fs) LA-MC-ICPMS in situ Pb, and bulk C—O—S isotope analyses, together with a detailed dataset of the ore deposit geology and mineralogy, aimed at revealing the ore genesis of the Fule deposit and its relationship with the ELIP. The outcomes will have wide significance for further exploration of carbonate-hosted Pb—Zn deposits in the ELIP and can open the door to similar situations in other Large Igneous Provinces where they interact with carbonate rocks.

2. Geological setting

2.1. Geology of the western Yangtze Block

The Yangtze Block is bounded by the Cathysia Block to the southeast, the Sanjiang Orogenic Belt to the southwest and the Songpan-Ganzê Orogenic Belt to the northwest (Fig. 1a). In the western Yangtze Block, the basement is comprised of late Paleoproterozoic to early Neoproterozoic metamorphic rocks, which were intruded by late Neoproterozoic and Mesozoic igneous rocks (Fig. 1b) (Gao et al., 2011; M.F. Zhou et al., 2014; Hu et al., 2017). The cover sequence in the western Yangtze Block is late Ediacaran to Triassic marine, and Jurassic to Cenozoic continental sedimentary rocks (Liu and Lin, 1999; Yan et al., 2003; Zhou et al., 2013a). The platform carbonate sequences constitute an important part of the late Ediacaran to Triassic marine strata, which are rich in salt-gypsum and organic matters (Huang et al., 2004; Jin, 2008; J.X. Zhou et al., 2014a). The western margin of the Yangtze Block is characterized by multiple processes of tectonic activity, which strictly controlled sedimentation, magmatism and mineralization (Figs. 1b, 2).

The late Permian ELIP (263–259 Ma) covers ~0.3 × 10^6 km^2 of the western Yangtze Block and eastern Songpan-Ganzê Orogenic Belt (Fig. 1a–b), with displaced correlative units in northern Vietnam (Song Da zone). It hosts many economically important Fe—Ti—V oxide deposits, Ni—Cu—(PGE) sulfide deposits and native Cu deposits (Zhou et al., 2002; Ali et al., 2005; Zhu et al., 2007; Jian et al., 2009; Shellnutt, 2014; Tran et al., 2016). The Emeishan flood basalts constitute a significant part of the ELIP, and are up to ~5 km maximum thickness in the western part of the ELIP (i.e. Yunnan), whereas the maximum thickness is only a few hundred meters in the eastern part (i.e. Guizhou) (Xu et al., 2001; Pirajno, 2013; Shellnutt, 2014). After eruption of the Emeishan basalts, the Indosinian Orogeny (257–200 Ma) resulted from closure of Paleotethys (Carter et al., 2001; Lepvrier et al., 2004; Enkelmann et al., 2007; Reid et al., 2007; Pullen et al., 2008; Qiu et al., 2016), resulting in faulting and folding that structurally controlled the occurrence of hydrothermal deposits in the western Yangtze Block (Fig. 1b) (Liu and Lin, 1999; Zaw et al., 2007; Zhu et al., 2007; Hu and Zhou, 2012; Chen et al., 2015).

The SYG Pb—Zn metallogenic province covers ~0.2 × 10^6 km^2 of SW Sichuan, NE Yunnan and NW Guizhou provinces (Fig. 1a), and hosts 408 carbonate-hosted Pb—Zn deposits in late Mesoproterozoic to late Paleozoic, all of which are spatially associated with the late Permian Emeishan basalts (Fig. 1b) (Liu and Lin, 1999; Zhou et al., 2013a; Wang et al., 2014; Zhang et al., 2015; Hu et al., 2017). These deposits were formed between 245 Ma and 192 ± 7 Ma as constrained by Pb model ages, and hydrothermal calcite/fluorite Sm-Nd and sphalerite/pyrite Rb-Sr isochron dating (Guan and Li, 1999; Si et al., 2006; Li et al., 2007; Lin et al., 2010; Mao et al., 2012; Zhou et al., 2013a,

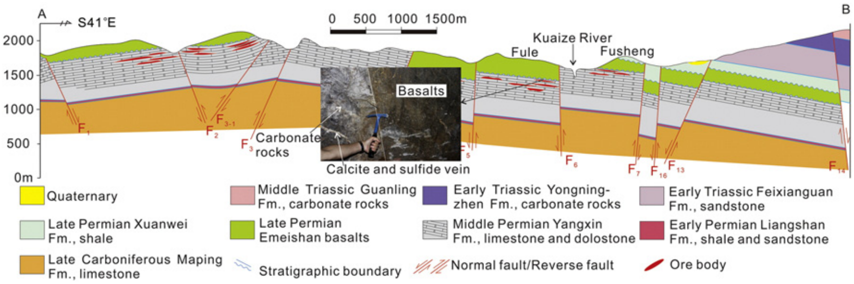

Fig. 3. A–B cross-section through the Fule district (modified from Liu and Lin, 1999), revealing the distribution of ore bodies, faults and strata, and the spatial relationship between sulfide ores and basalts.

2013b, 2015; Zhang et al., 2015). These dates broadly match the ages of basalt-hosted native Cu deposits in the ELIP (231 ± 3–225 ± 2 Ma: Zhu et al., 2007), Carlin-like Au deposits in the Youjiang Basin (235 ± 33–204 ± 19 Ma: Chen et al., 2015) and detritus (~230–206 Ma) in the Songpan-Ganzê Orogenic Belt that resulted from collision with the western Yangtze Block during the late Triassic (Enkelmann et al., 2007).

2.2. Regional geology of the Fule district

The Fule carbonate-hosted Pb—Zn deposit is located 110 km NE of Luoping City, NE Yunnan Province (Fig. 1b). The exposed rocks include the Mesoproterozoic Kunyang Group basement rocks, and late Paleozoic (middle Devonian, Carboniferous and Permian) and early Mesozoic (early-middle Triassic) cover sequences (Si et al., 2006; Lu et al., 2015). The Kunyang Group is composed mainly of mudstone and metasandstone, which are unconformably overlain by the middle Devonian Haikou Formation that consists mainly of limestone and sandstone. The Haikou Formation sedimentary rocks are unconformably overlain by early Carboniferous coal-bearing clastic rocks and late Carboniferous carbonate rocks. Sedimentary rocks of Carboniferous age are conformably overlain by early Permian limestone, shale and sandstone, which are in turn conformably overlain by limestone and dolostone of middle Permian Yangxin Formation. Carbonate rocks of the Yangxin Formation are disconformably overlain by late Permian, which consists mainly of Emeishan basalts, and coal-bearing clastic rocks. Late Permian clastic rocks are conformably overlain by early Triassic sandstone, mudstone and carbonates, which are in turn overlain conformably by middle Triassic carbonates.

The Mile-Shizong-Shuicheng fault (Fig. 1a) and Faben anticline (Si et al., 2011; Lu et al., 2015) form major structural features in the studied district. The Mile-Shizong-Shuicheng regional fault strikes NE-SW, with a slight bend in the Fule district (Fig. 1b). It consists of a series of secondary fractures that controlled the distribution of Pb—Zn deposits (Figs. 2–3) (Liu and Lin, 1999; Zhou et al., 2013b; Qiu et al., 2016). The Faben anticline is 20 km in length and 10 km wide, and is a gentle fold structure whose axis strikes 030–040° (Si et al., 2006). Carboniferous rocks in the central part of the anticline have a horizontal dip angle, whereas Permian rocks dip at 5°–10°. The Emeishan flood basalts are widely distributed in the Fule district, but their thickness is relatively thin, as they form the southeastern margin of the ELIP (Liu and Lin, 1999; Xu et al., 2001; Pirajno, 2013; Shellnutt, 2014).

More than 10 Pb—Zn ore deposits have been discovered over ~60 km^2 in the Fule district (Fig. 2), including the Fule (~10 Mt of sulfide ore with mean grades of 15–20 wt% Zn + Pb), Fusheng (~3 Mt of sulfide ore with average grades of 15–25 wt% Zn + Pb) and Fuli (~1 Mt of sulfide ore with mean grades of 10–15 wt% Zn + Pb) deposits (Si et al., 2006; Lu et al., 2015). All the Pb—Zn deposits are hosted by carbonate rocks of the middle Permian Yangxin Formation (Figs. 2–3). Ore bodies occur as stratiform or lentiform shapes along bedding-planes (Fig. 3), and are structurally controlled by the regional fault-fold system (Figs. 1b, 2–3). A principal feature of these deposits is that they are rich in Ag, Cu, Cd, Ge and Ga (Si et al., 2006; Ye et al., 2011; Zhu et al., 2017).

3. Geology of the Fule ore deposit

3.1. Stratigraphy and lithology

In the Fule mining area, the exposed lithologies include Permian, early-middle Triassic and Quaternary rocks (Figs. 2–3). The late Carboniferous Maping Formation was exposed by underground mining tunnels (Fig. 3), and consists mainly of dolomitic bioclastic limestone. The Maping Formation limestone is conformably overlain by the early Permian Liangshan Formation that is mainly composed of limestone, shale and sandstone. Sedimentary rocks of the Liangshan Formation are conformably overlain by carbonate rocks of the middle Permian Yangxin Formation, which are in turn disconformably overlain by late Permian Emeishan flood basalts. The basalts are disconformably overlain by the terrestrial coal-bearing clastic sequence of the late Permian Xuanwei Formation. Clastic rocks of the Xuanwei Formation are conformably overlain by the early Triassic Feixianguan Formation, which consists mainly of sandstone, shale and argillaceous limestone. The Feixianguan Formation sedimentary rocks are conformably overlain by the early Triassic Yongzhenning Formation that is composed mainly of carbonate rocks, which are in turn conformably overlain by oolitic dolostone and limestone of the middle Triassic Guanling Formation. Quaternary sediments locally overlie the Permian and Triassic rocks (Figs. 2–3).

3.2. Structural geology

The major structures in the Fule mining area include secondary structures of the Mile-Shizong-Shuicheng regional fault and the right limb of the Faben anticline (Fig. 1b, and see Figs. 2–3 for the details). The F_4 fault is a normal structure and strikes 000°–030° with a length of 43 km (Figs. 2–3). The F_5 fault is a reverse fault and trends 000–045° and is 17 km long (Figs. 2–3). Another important fault, the F_6 reverse fault (Fig. 4a), is 20 km in length and strikes 000–050° (Figs. 2–3). The F_5 and F_6 reverse faults controlled the occurrence of the Pb—Zn ore bodies in the Fule mining area (Figs. 2–3).

3.3. Magmatic rocks

The Emeishan flood basalts are the only igneous rocks exposed in the Fule mining area, and have a close spatial association with all the known Pb—Zn deposits (Figs. 2–3). The distance between the basalts and Pb—Zn ores is <1 m locally (Fig. 3).

3.4. Ore bodies

Twenty-ore bodies have been discovered in the Fule deposit, all of which are buried, and these have a total NW-SE length of 3000 m and NE-SW width of 1500 m. They have been divided into the Laojuntai and Xinjuntai sections, with the Laojuntai section having been completely mined-out (Si et al., 2011). Ore bodies in the Xinjuntai section occur as stratiform to lentiform shapes or as veins along bedding-planes within the Yangxin Formation; they trend SE with a dip of 10° (Fig. 3). The Erdong stratiform ore body is the largest one in the Xinjuntai section, and is 1000 m in length, 300–500 m in width and 0–20 m in thickness. The next largest is the Danaotang ore body, which is lenticular and 500 m long, 400 m wide and 0–20 m thick. These large ore bodies have also been completely mined-out. The total mined-out sulfide ore in the two sections are >7 Mt (Si et al., 2013). Some medium-scale ore bodies have been found recently, for example, the No. 108 stratiform ore body, which is 400 m long, 200 m wide and 2–12 m thick; the No. 904 lentiform ore body, which is 340 m in length, 200 m in width and 1.5–15 m in thickness; and the No.74 veined ore body, which is 200 m long, 150 m wide and 3–15 m thick. Sulfide ore in these newly-discovered ore bodies contains Zn + Pb grades up to 60 wt%, averaging 15–20 wt%, and 256–8171 μg/g Cd, 1.77–239 μg/g Ge, 0.74–182 μg/g Ga, 23.5–107 μg/g Se, and 0.98–122.1 g/t Ag. The total metal reserves of Cd, Ge and Ga are >4567 t, 329 t and 177 t, respectively (Si et al., 2006, 2011, 2013; Zhu et al., 2017).

3.5. Structure and texture of the sulfide ores

Previous studies showed that sulfide ore in the Fule deposit is composed mainly of sphalerite, galena and pyrite, with calcite and dolomite as gangue minerals (Figs. 4–7). In this study, Cu and Ni sulfide minerals, together with apatite (Fig. 7f), have been identified,

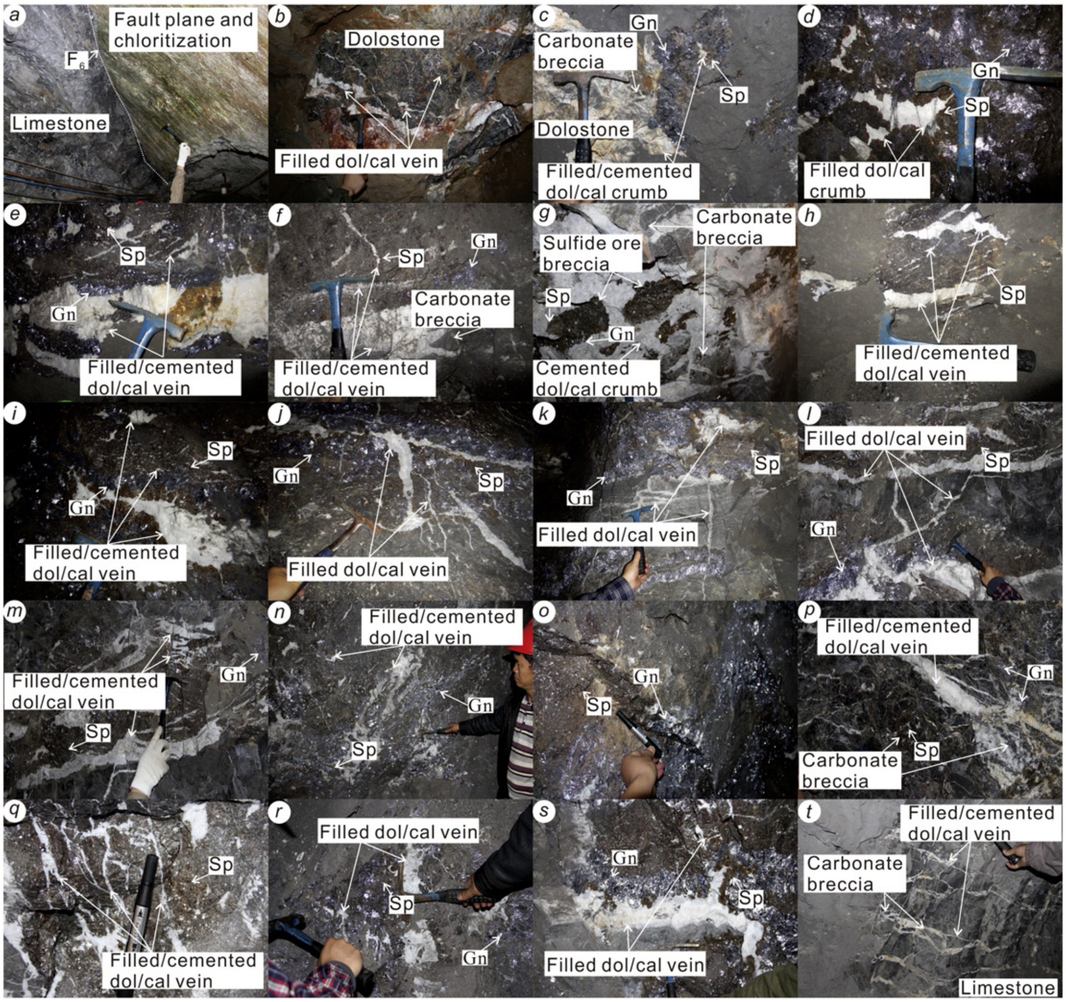

Fig. 4. Field photographs of the Fule deposit; a: F_6 reverse fault plane with chloritization; b: post-ore dolomite/calcite (Dol/Cal) veins fill fractures in dolostone; c: sphalerite (Sp) and galena (Gn) occur as massive aggregates that are filled by Dol/Cal crumbs, and carbonate breccias are cemented by Dol/Cal veins; d: Dol/Cal occur as crumbs and fill fractures in massive Sp and Gn aggregates; e: massive Sp and Gn aggregates are filled/cemented by Dol/Cal veins; f: massive Sp and Gn, and carbonate breccias are filled/cemented by Dol/Cal veins; g: breccias of sulfide ore and carbonate are cemented by Dol/Cal crumb aggregates; h: interbedded sulfide veins are filled/cemented by Dol/Cal veins or veinlets; h–n: massive Sp and Gn are filled/cemented by Dol/Cal veins; o: massive Sp and Gn; p: Dol/Cal veins fill fractures in the wall rocks or cement carbonate breccias, and Sp and Gn occur as speckles or single crystals that are irregularly distributed in the wall rocks; q–r: massive Sp and/or Gn are filled/cemented by Dol/Cal veins; t: post-ore Dol/Cal veins fill fractures in the wall rocks or cement the carbonate breccias.

including tetrahedrite (Figs. 6g, k, m, t and 7g–h, j, l–s), chalcopyrite (Fig. 6i, r–t), millerite, polydymite, and pentlandite (Fig. 7s).

The main sulfide minerals occur as either massive (Figs. 4c–f, h–o, q–s and 5a, e, k–q), veined (Figs. 4h, 5b–d, i–j, r–t and 6a–c), disseminated (Figs. 4p and 5g–h, n, r–s) or brecciated (Figs. 4g, 5f and 6d) structure. Aggregations of sulfide minerals in the wall rocks form massive ore (Figs. 4c–e, i–j, n–o and 5a, k); sulfide veins between millimeter-scale veinlets (Figs. 4h, 5b–d and 6a) or centimeter-scale veins of calcite/dolomite (Figs. 5i–j, r–t and 6b–c) constitute the veined ore, whereas in the disseminated ore, sulfide minerals occur as speckles or single crystals irregularly distributed in the wall rocks (Fig. 4p) or in calcite/dolomite veins (Fig. 5g–i, n, r–s). In the brecciated ore, fragments of sulfides and carbonate rocks are enclosed in calcite/dolomite cements (Figs. 4g and 5f).

The hydrothermal minerals occur in a variety of forms and may be granular (Figs. 6e–t and 7a–t), form replacement minerals (Fig. 6r), have embayments (Figs. 6f, l, s and 7b, d, j, m), occur in solid-solution (Figs. 6i, s and 7a–b, d, k, o, s), show stress deformation (Figs. 6e–f, l–m and 7g–h) or have cataclastic textures (Fig. 6n). Granular form is common and sphalerite occurs as euhedral to anhedral fine- (<0.5 mm, Figs. 6e–f, h, j–m, o–r, t and 7a, c, h–i, p), medium- (0.5–5 mm, Fig. 6g, k–l and 7a–d, q) to coarse-grained minerals (>5 mm, Figs. 5i, n, r–s, 6b–d, i, s and 7t); Galena is euhedral to anhedral, fine- to coarse-grained with grain sizes of 0.01–15 mm (Figs. 5k, 6c, e–f, l–m and 7a–h, j, i–t). Stress deformation is a common feature in galena (Figs. 6e–f, l–m and 7g–h). Chalcopyrite has a solid-solution texture within sphalerite (Fig. 6i, s) or else replaces pyrite (Fig. 6r). The contacts between sphalerite and galena (Fig. 6f, l) or calcite/dolomite (Fig. 6s and 7b, d, j, m) commonly show embayment. Pyrite has commonly has a cataclastic texture (Figs. 6h, n and 12). In contrast, millerite and pentlandite occur as a solid-solution in polydymite (Fig. 7s), whereas calcite and dolomite often form solid-solutions (Fig. 7a–b, d, k, o, s).

3.6. Mineral paragenesis

Based on macro-scale geological observations, microscope identification and scanning electron microscopy (SEM) analysis, together with previously published geological data (Si et al., 2006, 2011), the ore-forming process of the Fule deposit can be divided into diagenetic, hydrothermal and supergene periods (Fig. 8). The hydrothermal period can be further divided into sulfide + carbonate (including two generations, i.e. I and II) and barren carbonate (includes one generation, namely III) stages (Fig. 8). There are two principal sulfide ore types: sphalerite-dominated (Figs. 4h, q, 5a–j, p–t and 6a–c) and sphalerite + galena-dominated (Figs. 4c–f, i–p,

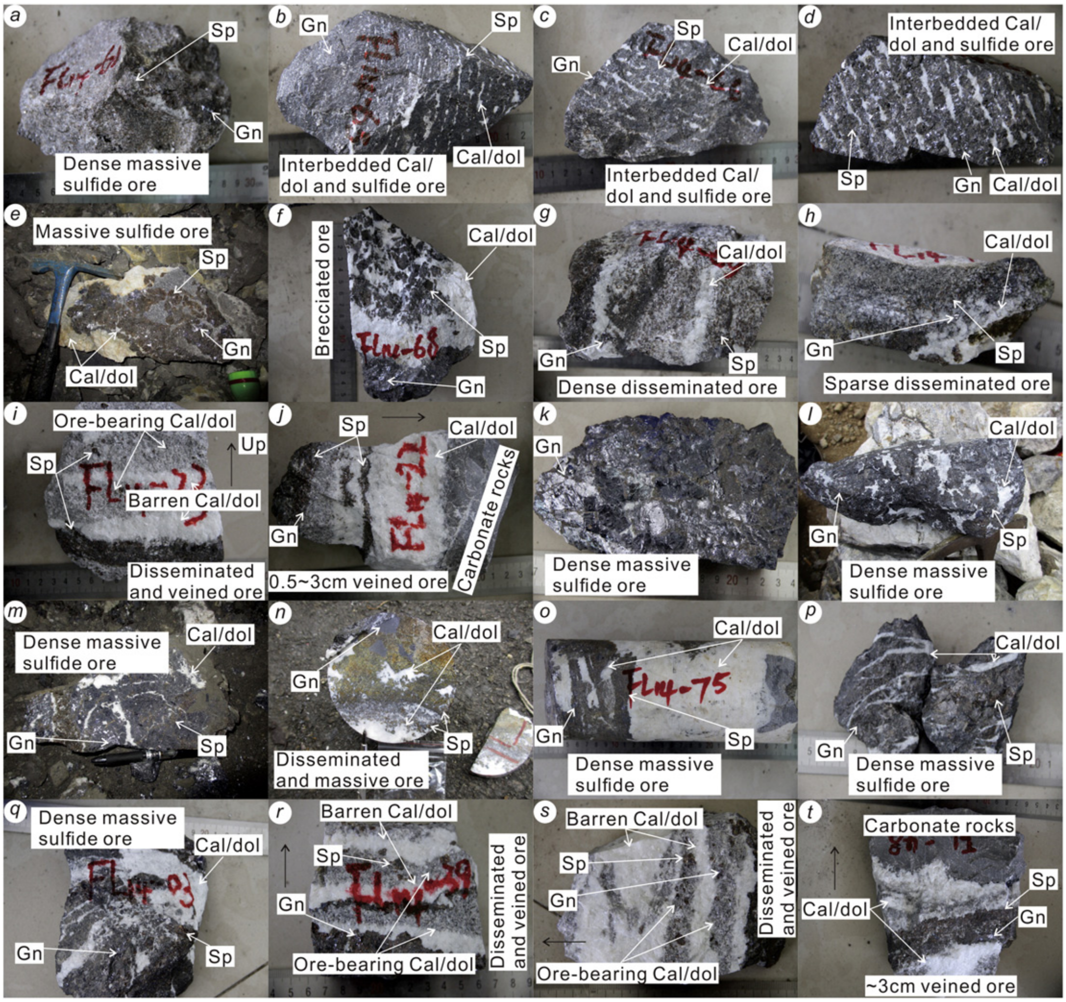

Fig. 5. Photographs of hand specimens from the Fule deposit; a: dense massive sulfide ore, sphalerite (Sp) coexists with galena (Gn); b–d: interbedded sulfide veins between calcite/dolomite (Cal/Dol) millimeter-scale veinlets; e: massive Sp and Gn are filled/cemented by Cal/Dol crumbs, veinlets or veins; f: sulfide ore breccias are cemented by Cal/Dol aggregates; g–h: Sp and Gn occur as speckles or single crystals that are either densely or sparsely distributed in dolostone, which is filled by Cal/Dol veins; i–j: Sp and Gn occur as speckles or single crystals that are distributed in Cal/Dol aggregates, which are filled by barren Cal/Dol veins; these barren veins and sulfide veins together form veined ore; k: Gn occurs as massive aggregates; l–m: massive Sp and Gn are filled by Cal/Dol fragments or veinlets; n: Cal/Dol fragments fill fractures in the massive Sp and Gn ores or host disseminated Sp; o–q: massive Sp and Gn are filled by Cal/Dol fragments or veinlets; r–t: barren Cal/Dol, speckles or single crystals of Sp and/or Gn-bearing Cal/Dol and sulfide veins form veined ore.

r–s, 5k–o and 6d). These two ore types have the following spatial distribution from bottom to top as follows: massive sphalerite-dominated ore often occurs at the bottom of the ore body (Fig. 4j, m, o, q), followed by massive sphalerite + galena-dominated (Figs. 4c–f, i–p, r–s and 5n) or sphalerite-dominated interbedded veins (Figs. 4h, 5b–d, i–j, r–t and 6a–c), with disseminated sphalerite + galena-dominated ore commonly at the top (Figs. 4p and 5g–j, n, r–s).

Overall, there are at least two generations of hydrothermal minerals formed in the two types of sulfide ore. Sphalerite-I is euhedral (Figs. 5e, h, j, o, r and 6i) to anhedral (Figs. 5f–g, k–n and 6a–e) fine- to medium-grained (0.01–0.5 mm), coexisting with galena-I (Figs. 6a–c and 7a, q), pyrite-I (Figs. 6k, 7e and 10), tetrahedrite (Figs. 6m and 7h, q) or calcite/dolomite-I (Figs. 6a–c and 7a–b), and is enclosed by galena-II (Figs. 6f, l–m and 7h, l), as well as being filled by galena-II (Fig. 6g, q and 7g, t), tetrahedrite (Figs. 6h and 7g), pyrite-II (Fig. 6n), calcite/dolomite-II (Figs. 6g, k, n, q and 7a, e) or replaced by chalcopyrite (Fig. 6i). Sphalerite-II occurs as subhedral to anhedral medium- to coarse-grained crystals (0.5–10 mm) that coexist with galena-II (Figs. 6e–f, l, p, r and 7h, j, l, p, r), pyrite-II (Figs. 6h, r and 7c–d), tetrahedrite (Fig. 6t and 7l, p, r), chalcopyrite (Fig. 6r) or calcite/dolomite-II (Fig. 6e–f, p, s–t), and are enclosed by calcite/dolomite-II (Figs. 6h, j, o, r and 7i). Galena-I is euhedral to anhedral fine- to medium-grained (0.01–0.1 mm), and coexists with sphalerite-I (Figs. 6a–c and 7a, q), pyrite-I (Fig. 7e) or calcite/dolomite-I (Figs. 6a–c and 7a), and is enclosed by pyrite-II (Fig. 7c–d) or calcite/dolomite-II (Fig. 7e, m, o). Galena-II forms subhedral to anhedral medium- to coarse-grained crystals (0.1–15 mm) that coexist with sphalerite-II (Figs. 6e–f, l, p, r and 7h, j, l, p, r), tetrahedrite (Figs. 6g and 7l–m, o–p), or calcite/dolomite-II (Figs. 6e–g, p–r and 7m–o), and enclose sphalerite-I (Figs. 6f, l–m and 7h, l), pyrite-I (Figs. 6r and 7n) or tetrahedrite (Figs. 6m and 7h, j, n, r), as well as filling sphalerite-I (Figs. 6g, q and 7g, t). Pyrite-I coexists with sphalerite-I (Figs. 6k, 7e and 11) or galena-I (Fig. 7e), and is enclosed by galena-II (Figs. 6r, and 7n) or calcite/dolomite-II (Fig. 7e). Pyrite-II coexists with sphalerite-II (Figs. 6h, r and 7c–d) or calcite/dolomite-II (Figs. 6h, n, r and 7c–d), and encloses galena-I (Fig. 7c–d), as well as being replaced by chalcopyrite (Fig. 6r). Syn-ore calcite/dolomite-I occurs as crumbs or millimeter-scale discrete veinlets that enclose or coexist with sphalerite-I and galena-I (Figs. 6a–c and 7a–b). Syn-ore calcite/dolomite-II forms centimeter-scale veins (Figs. 5i–j, r–t and 6b–d) that fill, cement or coexist with two generations of sulfide minerals (Figs. 6–7). Post-ore calcite/dolomite-III occurs as veinlets or stockworks that fill fractures in the sulfide ores (Figs. 4e–g and 6a) or cement carbonate breccias

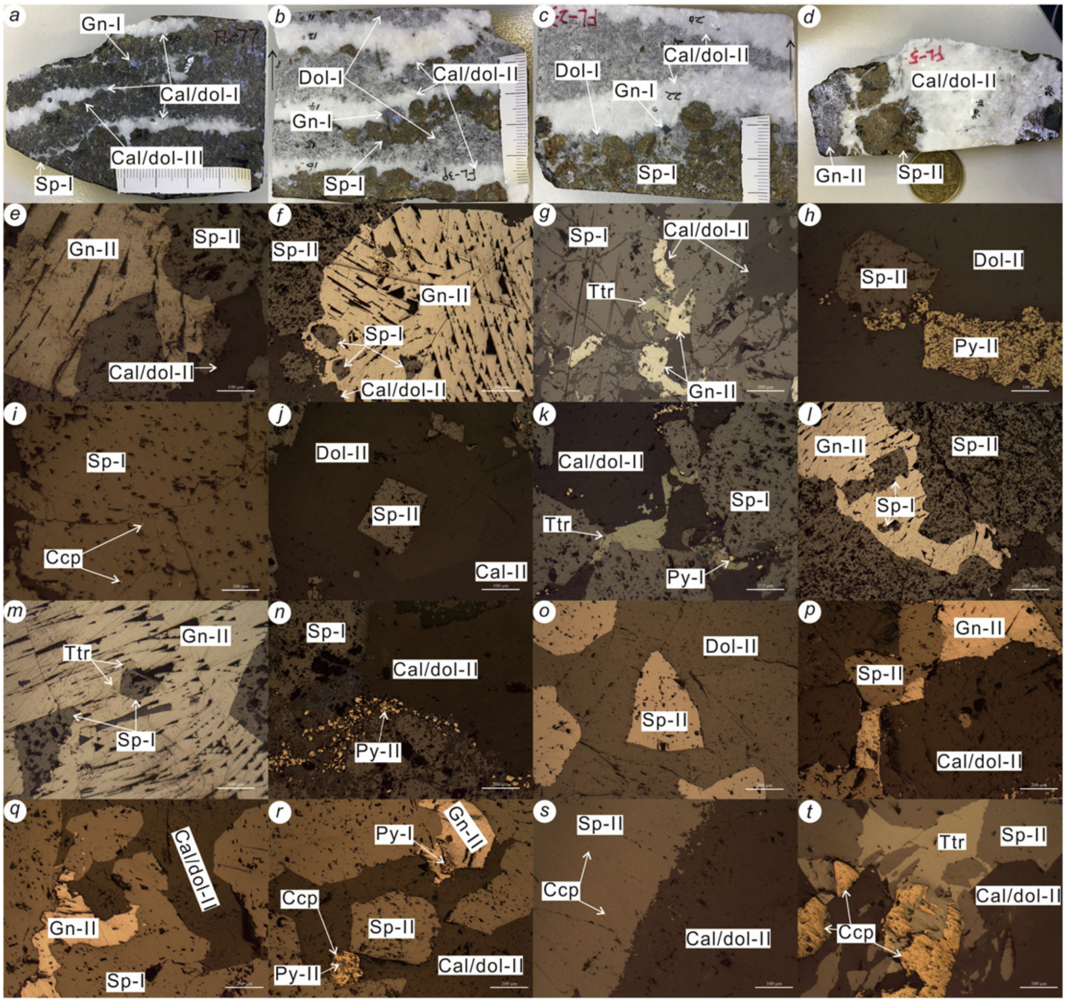

Fig. 6. The textural and structural features of sulfide minerals in the Fule deposit under the microscope; a: sphalerite-I (Sp-I) coexists with galena-I (Gn-I), and forms veined aggregates; calcite/dolomite-I (Cal/Dol-I) forms veined aggregates and is interbedded with sulfide veins; post-ore Cal/Dol-III fills fractures in the sulfide veins; b–c: barren Cal/Dol-II, disseminated sulfide-bearing Dol-I, and Sp-I and Gn-I veins form veined ore; d: massive Sp-II and Gn-II are filled by Cal/Dol veins; e: Sp-II occurs as euhedral to anhedral fine-grained crystals and coexist with Gn-II; f: Gn-II forms subhedral medium-grained crystals that enclose Sp-I and coexist with Sp-II; g: Sp-I forms granular crystals that are filled by Cal/Dol-II, Gn-II, and tetrahedrite (Ttr); h: granular Sp-II coexists with granular Py-II, both of which are enclosed by Dol-II; i: Chalcopyrite (Ccp) occurs as within Sp-I; j: Sp-II forms a euhedral fine-grained crystal that is enclosed by Dol-II and Cal-II; k: anhedral Sp-I coexists with Py-I and Ttr, all of which are cemented by Cal/Dol-II; i: Gn-II forms a subhedral fine-grained crystal that encloses Sp-I and coexists with Sp-II; m: fine-grained Sp-I crystal coexists with Ttr and is enclosed by coarse-grained Gn-II crystal; n: fine-grain cataclastic Py-II crystals coexist with Cal/Dol-II, both of which fill fractures in the Sp-I; o: Sp-II forms a subhedral fine-grained crystal and is enclosed by Dol-II; p: Sp-II coexists with Gn-II and Cal/Dol-II; q: Sp-I is filled by Gn-II and Cal/Dol-II; r: Gn-II encloses Py-I and coexists with Sp-II, and Py-II replaces Ccp, all of which are filled/cemented by Cal/Dol-II; s: Ccp occurs within Sp-II that forms an embayment texture with Cal/Dol-II; t: Ccp coexists with Ttr and Sp-II, all of which are filled or enclosed by Cal/Dol-II.

(Fig. 4b, t). In addition, millerite and pentlandite coexists with galena-I and all are enclosed by polydymite (Fig. 7s). Apatite occurs as euhedral crystal and is enclosed by dolomite-III that fills fractures in galena-II (Fig. 7f).

3.7. Wall rock alteration

Wall rock alteration includes chloritization and carbonatization, which can be divided into pre- and post-ore stages. The pre-ore stage of chloritization generated chlorite along fault planes within the basalts (Fig. 4a), and carbonatization recrystallized coarse-granular dolostone (Fig. 4b–c). The post-ore stage is of carbonatization forming barren carbonate (dolomite and calcite) veins or veinlets, which cement/fill fractures within sulfide ore (Figs. 4e–g and 6a) or wall rocks (Fig. 4b, t). The pre-ore chloritization/carbonatization, resulted from water/rock interaction between fluids and basalts/carbonates, usually occur along fluid migration pathways. The post-ore alteration is always close to sulfide ore, and thus can be used as a clue in mineral exploration.

4. Samples and analytical methods

4.1. Samples

Sulfide ore samples were collected mainly from the newly-discovered ore bodies, because the other main ore bodies had been mined-out completely (Si et al., 2011). Seven calcite and ten sulfide mineral separates were handpicked from seventeen sulfide ore samples, which were used for bulk C—O and S isotope analyses, respectively. Four fresh limestone samples were also used for bulk C—O isotope analysis. Twelve polished thin sections of sulfide ores were used for NanoSIMS in situ S and Fs-LA-MC-ICPMS in situ Pb isotope analyses. In situ δ^{34}S values for galena were not obtained, because no galena standard was available (Tang et al., 2014; Zhang et al., 2014). Also, no in situ Pb isotopic ratios of pyrite and sphalerite were obtained as their high Hg contents could markedly affect the quality of the data (Chen et al., 2014; Bao et al., 2016, 2017; Tan et al., 2017).

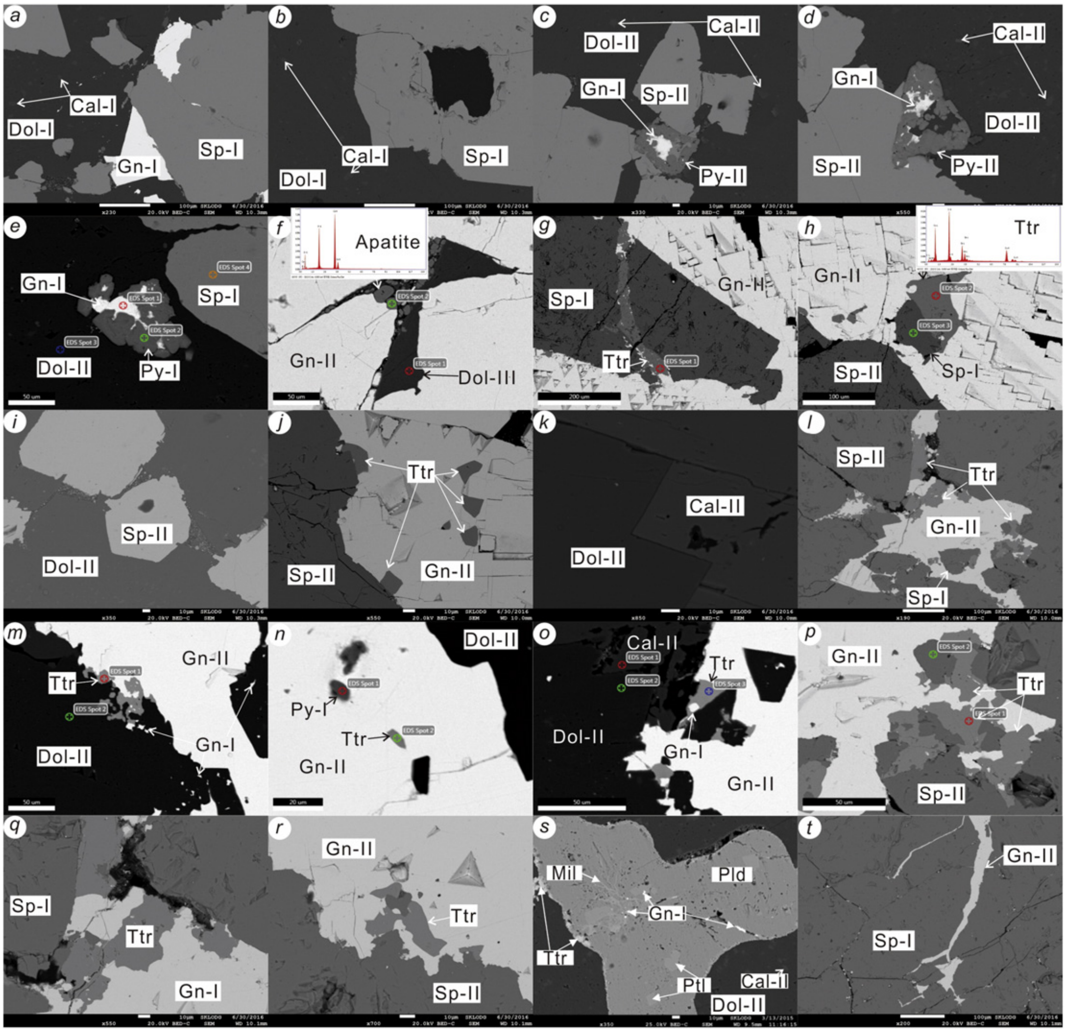

Fig. 7. The texture and structure of hydrothermal minerals in the Fule deposit under the scanning electron microscope (SEM); a: Sphalerite-I (Sp-I) present as euhedral-subhedral fine- to medium-grained crystals that coexist with galena-I (GnI), all of which are filled or enclosed by dolomite-I (Dol-I) that forms a solid-solution with calcite-I (Cal-I); b: Sp-I occurs as a medium-grained crystal and forms embayment texture with Dol-I that encloses Cal-I solid-solution; c: Py-II encloses Gn-I and coexists with Sp-II, both of which form embayment texture with Cal-II; e: Py-I and Gn-I are enclosed by Dol-II that fills a fracture in the Sp-I; f: apatite is enclosed by Dol-III that fills a fracture in Gn-II; g: Gn-II and Ttr fill a fracture in Sp-I; h: Ttr occurs as a fine-grained crystal that coexists with fine-grained Sp-I, all of which are enclosed by coarse-grained Gn-II that coexists with Sp-II; i: Sp-II occurs as a euhedral fine-grained crystal that is cemented or enclosed by Dol-II; j: Gn-II encloses Ttr and coexists with Sp-II; k: solid-solution texture of Dol-II and Cal-II; l: Gn-II encloses Sp-I and coexists with Ttr and Sp-II; m: Gn-II coexists with Ttr and Dol-II, of which the latter encloses Gn-I; n: Dol-II coexists with Gn-II that encloses Py-I and Ttr; o: Ttr encloses Gn-I and coexists with Gn-II and Dol-II, of which the latter forms a solid-solution texture with Cal-II; p: Gn-II coexists with Ttr and Sp-II; q: Sp-I coexists with Gn-I and Ttr; r: Gn-II forms embayment texture with Sp-II and coexists with Ttr; s: Ttr occurs as aggregate veinlets along the rim of polydymite (Pld); millerite (Mil) occurs as a micro-vein aggregate within Pld; pentlandite (Ptl) is a euhedral fine-grained crystal within Pld; Gn-I coexists with Ptl; all of them are enclosed by Dol-II that encloses Cal-II solid-solution; t: Gn-II forms fine veinlets and fills fractures in Sp-I.

4.2. Analytical methods

4.2.1. Bulk C—O isotope analysis

Bulk C—O isotope analysis was performed at the State Key Laboratory of Ore Deposit Geochemistry (SKLODG), Institute of Geochemistry (IG), Chinese Academy Sciences (CAS), using a Finnigan MAT-253 mass spectrometer. Calcite separates and limestone whole-rock reacted with 100% H_3PO_4 to produce CO_2. The analytical precisions calculated from replicate analyses of unknown samples were better than 0.2‰ (2σ) and 1‰ (2σ) for $\delta^{13}C$ and $\delta^{18}O$, respectively. The $\delta^{13}C$ and $\delta^{18}O$ values were reported relative to the Vienna Pee Dee Belemnite (V-PDB) standard and Standard Mean Ocean Water (SMOW), respectively.

4.2.2. In situ S isotope analysis

In situ S isotope analysis was undertaken at the Key Laboratory of Earth and Planetary Physics, Institute of Geology and Geophysics, CAS, using a CAMECA NanoSIMS. The measurements were made using 3 different settings of the Faraday cups/electron multiplier (EM) detectors, in order to meet the diverse requirements for spatial resolution. The standard-sample-standard bracketing method was applied to correct for instrumental mass fractionation. Target spots of the most homogeneous isotopes (such as ^{32}S, ^{34}S and ^{75}As in Fig. 9) were selected for in situ S isotope analysis in order to obtain the most credible data. Internal standards included PY-1117 (pyrite), CS01 (pyrite), JC-14 (sphalerite) and MY09-12 (sphalerite), and international standards included Balmat (pyrite and sphalerite) and CAR 123 (pyrite). The analytical precision calculated from replicate analyses of the unknown samples was better than 0.2‰ (1σ). The in situ S isotopic compositions were reported relative to the Vienna Canyon Diablo Troilite (V-CDT) standard. Details of instrument parameters and NanoSIMS in situ S isotope analysis techniques were described in Zhang et al. (2014).

4.2.3. Bulk S isotope analysis

Bulk S isotope analysis was undertaken at the SKLODG, IGCAS, using a Finnigan MAT-253 mass spectrometer. Sulfide mineral powders (200 mesh) were mixed with CuO powder, and then were heated to extract SO_2. The analytical uncertainty was better than 0.1‰ (1σ)

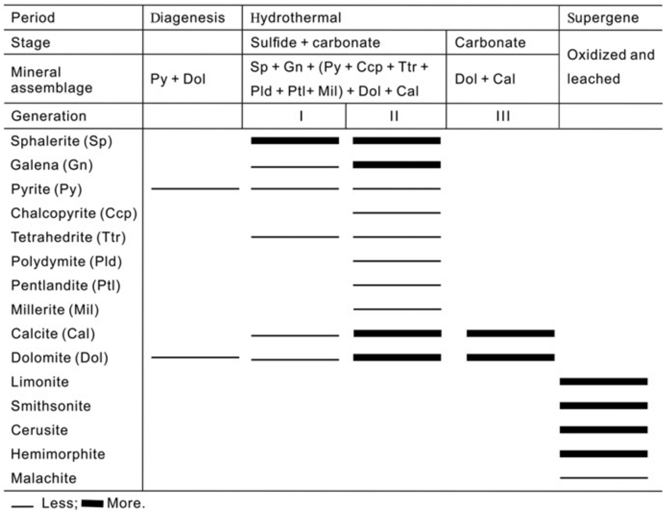

Fig. 8. Mineral paragenesis in the Fule Pb—Zn deposit (data are sourced from Si et al., 2006 and this paper).

calculated from replicate analyses of the IAEA international standards: IAEA S1 (−0.3‰), IAEA S2 (+22.62‰) and IAEA S3 (−32.49‰). The analytical precision calculated from replicate analyses of the unknown samples is better than 0.2‰ (2σ). The bulk δ^{34}S values are reported relative to the Vienna Canyon Diablo Troilite (V-CDT) standard.

4.2.4. In situ Pb isotope analysis

In situ Pb isotopes were analyzed at the State Key Laboratory of Continental Dynamics, Northwest University, using a Nu II MC-ICPMS instrument combined with a 266 nm femtosecond (fs) laser ablation system. The surface of the polished thin sections was cleaned with milli-Q water (18.2 MΩ·cm). Line scan ablation consisted of background collection for 20 s followed by 50 s of laser ablation for signal collection. Laser ablation parameters were: 15 μm spot size for galena; 100% output energy, >600 μJ; 100% energy density, 6 J/cm^2; laser frequency, 5–50 Hz; and ablation way, line 3 μm/s. These ensured a strong enough Pb signal for the in situ analysis of galena samples. The Tl (20 ppb), NIST SRM 997 (^{205}Tl/^{203}Tl = 2.38890) and NIST SRM 610 glass served as internal and external standards. The repeated analyses of NIST SRM 610 glass yielded highly reliable and reproducible results during the whole analytical process with mean ^{206}Pb/^{204}Pb = 17.052 ± 0.003, ^{207}Pb/^{204}Pb = 15.515 ± 0.003 and ^{208}Pb/^{204}Pb = 36.980 ± 0.007 (1 s, n = 183). Details of instrument parameters and fs LA-MC-ICP-MS in situ Pb isotope analyses were described in Bao et al. (2016).

5. Analytical results

5.1. Bulk C—O isotopic compositions

Bulk δ^{13}C and δ^{18}O values of syn-ore calcite separates and fresh limestone whole-rock samples are listed in Table 1 and are shown in Fig. 10. Syn-ore calcite (generation II) separates have δ^{13}C and δ^{18}O values ranging from +2.57 to +3.01‰ and +16.83 to +19.92‰, respectively. δ^{13}C and δ^{18}O values of fresh limestone whole-rock samples range from +1.58 to +2.63‰ and +21.85 to +24.01‰, respectively. The δ^{13}C values of syn-ore calcite can be compared with those of fresh limestone, but the former has slightly lower δ^{18}O values than those of the latter (Fig. 10).

5.2. In situ and bulk δ^{34}S values

In situ and bulk δ^{34}S values are presented in Table 2 and are shown in Figs. 11–12. The NanoSIMS in situ δ^{34}S values of sulfide minerals range from +9.8 to +23.1‰, of which pyrite and sphalerite crystals have δ^{34}S values ranging from +10.3 to +19.4‰ and +9.8 to +23.1‰, respectively. In situ δ^{34}S values of pyrite-I and pyrite-II crystals range from +12.8 to +19.4‰ and +10.3 to +10.4‰, respectively. Sphalerite-I and sphalerite-II crystals have in situ δ^{34}S values ranging from +12.5 to +23.1‰ and +9.8 to +16.9‰, respectively. A principal feature of both pyrite and sphalerite crystals is that their δ^{34}S values decrease gradually from core to rim (pyrite: decreasing from +19.4 to +10.3‰; sphalerite: decreasing from +23.1 to +9.8‰; Figs. 11 and 12a). Sulfide minerals have bulk δ^{34}S values ranging from +10.04 to +16.43‰, of which sphalerite has δ^{34}S values (+14.16–+16.43‰) higher

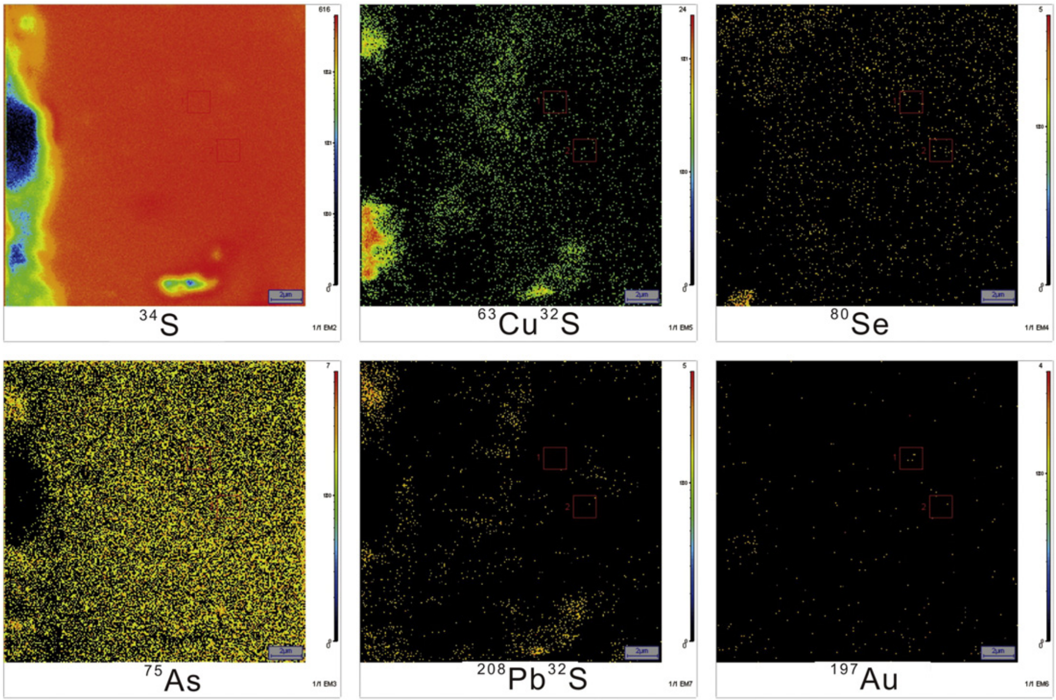

Fig. 9. The area selected for in situ S isotope analysis that has homogeneous isotopic compositions (including ^{32}S, ^{34}S, ^{75}As and ^{63}Cu^{32}S).

Table 1
C—O isotopic compositions of calcite and limestone in the Fule deposit.

No.	Locations	Mineral	$\delta^{13}C_{PDB}$/‰	$\delta^{18}O_{SMOW}$/‰	$\delta^{13}C_{CO_2}$/‰[a]	$\delta^{18}O_{H_2O}$/‰[b]
FL_{14}-2	Nos.108, 904 and 74 ore bodies	Calcite-II	+2.94	+16.84	+3.33	+7.81
FL_{14}-23		Calcite-II	+2.93	+19.92	+3.32	+10.89
FL_{14}-44		Calcite-II	+3.01	+18.15	+3.40	+9.12
FL_{14}-64		Calcite-II	+2.96	+19.77	+3.35	+10.74
FL_{14}-8		Calcite-II	+2.67	+16.86	+3.06	+7.83
FL_{14}-68		Calcite-II	+2.57	+16.83	+2.96	+7.80
FL_{14}-36		Calcite-II	+2.92	+18.25	+3.31	+9.22
FL_{14}-D1	The mining area periphery	Limestone	+1.85	+23.61		
FL_{14}-D2		Limestone	+1.58	+22.08		
FL_{14}-D3		Limestone	+2.18	+21.85		
FL_{14}-D4		Limestone	+2.63	+24.01		

t = 180–210 °C (av. 200 °C), based on temperature analysis of fluid inclusion in sphalerite-II (Li ZL, unpublished data).

[a] $1000\ln\alpha_{(CO_2-Calcite)} \approx \delta^{13}C_{CO_2} - \delta^{13}C_{Calcite} = -2.4612 + 7.663 \times 10^3 / (t + 273.15) - 2.988 \times 10^6 / (t + 273.15)^2$ (Bottinga, 1968).

[b] $1000\ln\alpha_{(Calcite-H_2O)} \approx \delta^{18}O_{Calcite} - \delta^{18}O_{H_2O} = 2.78 \times 10^6 / (t + 273.15)^2 - 3.39$ (O'Neil et al., 1969).

than those of galena (generation II: +10.04–+11.86‰). Sphalerite-I has bulk $\delta^{34}S$ values (+14.16–+16.43‰) similar to those of sphalerite-II (+14.21–+15.10‰). Another major feature is that bulk S isotopic data of sphalerite have a much narrower range than in situ S isotopic data (Fig. 11a–b).

5.3. In situ Pb isotopic compositions

In situ Pb isotopic ratios of galena are listed in Table 3 and are shown in Figs. 13–14. Galena (generation I and II) crystals have in situ $^{206}Pb/^{204}Pb$ ratios of 18.572–18.617, $^{207}Pb/^{204}Pb$ ratios of 15.711–15.728 and $^{208}Pb/^{204}Pb$ ratios of 38.592–38.727. In situ Pb isotopic ratios of galena-I are as follows: $^{206}Pb/^{204}Pb = 18.572$–$18.598$, $^{207}Pb/^{204}Pb = 15.711$–$15.728$ and $^{208}Pb/^{204}Pb = 38.592$–$38.695$ and in situ Pb isotopic ratios of galena-II are: $^{206}Pb/^{204}Pb = 18.580$–$18.617$, $^{207}Pb/^{204}Pb = 15.712$–$15.727$, and $^{208}Pb/^{204}Pb = 38.597$–$38.727$. The main feature is that $^{206}Pb/^{204}Pb$ and $^{208}Pb/^{204}Pb$ ratios of galena-I are lower than those of galena-II (Fig. 14a–b).

6. Discussion

6.1. Sources of ore-forming elements and associated fluids

6.1.1. New insights from C—O isotopes

Mineralogical records reveal that calcite and dolomite are the two main C-bearing minerals in the sulfide ores (Figs. 4–8). Thus, HCO_3^- and H_2CO_3 [occurring as CO_2 (aqueous)] are two dominant C species in the hydrothermal fluid, as supported by the analysis of fluid inclusions in sphalerite (Li ZL, unpublished data). Therefore, the calculated $\delta^{13}C_{CO_2}$ value is approximate to the theoretical $\delta^{13}C_{fluid}$ value, namely $\delta^{13}C_{CO_2} \approx \delta^{13}C_{fluid}$, if the fractionation of C isotopes between HCO_3^- (liquid) or H_2CO_3 and CO_2 (gas) is negligible (Ohmoto, 1972; Hoefs, 2009). The $\delta^{13}C_{CO_2}$ values were calculated using the temperature function of $1000\ln\alpha_{(CO_2-Calcite)} = -2.4612 + 7.663 \times 10^3 / (t + 273.15) - 2.988 \times 10^6 / (t + 273.15)^2$ (Bottinga, 1968; "t" [200 °C] is an average homogenization temperature of fluid inclusions in sphalerite, Li ZL, unpublished data). Similarly, the $\delta^{18}O_{H_2O}$ values were calculated using the temperature function of $1000\ln\alpha_{(Calcite-H_2O)} = 2.78 \times 10^6 / (t + 273.15)^2 - 3.39$ (O'Neil et al., 1969). We obtained $\delta^{13}C_{fluid}$ and $\delta^{18}O_{fluid}$ values having a range of +2.96–+3.40‰ and +7.80–+10.89‰, respectively (Table 2; Fig. 10).

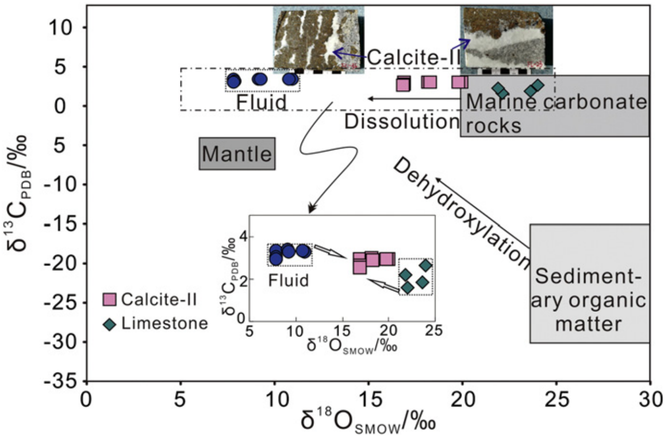

Fig. 10. Plot of $\delta^{13}C$ vs. $\delta^{18}O$; C—O isotopic data for mantle, marine carbonate rocks and sedimentary organic matters are sourced from Taylor et al. (1967), Demény et al. (1998), Veizer and Hoefs (1976) and Hoefs (2009).

It has been well-documented that $\delta^{13}C$ and $\delta^{18}O$ values of different geological reservoirs are distinct (Fig. 10). For instance, typical marine carbonate rocks have $\delta^{13}C$ values of −4–+4‰ and $\delta^{18}O$ values of +20–+30‰ (Veizer and Hoefs, 1976), the $\delta^{13}C$ and $\delta^{18}O$ values of mantle-derived CO_2 range from −8 to −4‰ and +6 to +10‰, respectively (Taylor et al., 1967; Demény et al., 1998), whereas sedimentary organic matters have $\delta^{13}C$ and $\delta^{18}O$ values mainly ranging from −30

Table 2
In situ and bulk S isotopic compositions of sulfide minerals in the Fule deposit.

No.	Locations	Mineral	$\delta^{34}S_{CDT}$/‰	Method
FL_{14}-3-01	Core	Pyrite-I	+18.7	In situ analysis
FL_{14}-3-02	Core	Pyrite-I	+19.3	
FL_{14}-10-01	Core	Pyrite-I	+17.7	
FL_{14}-10-02	Core	Pyrite-I	+17.8	
FL_{14}-25-01	Core	Pyrite-I	+19.3	
FL_{14}-25-02	Core	Pyrite-I	+19.4	
FL_{14}-60-01	Core	Pyrite-I	+17.5	
FL_{14}-60-02	Core	Pyrite-I	+18.0	
FL_{14}-60-03	Rim	Pyrite-I	+13.8	
FL_{14}-60-04	Rim	Pyrite-I	+13.2	
FL_{14}-65-01	Rim	Pyrite-II	+10.4	
FL_{14}-65-02	Rim	Pyrite-II	+10.3	
FL_{14}-65-03	Rim	Sphalerite-II	+9.8	
FL_{14}-65-04	Rim	Sphalerite-II	+10.1	
FL_{14}-65-05	Core	Sphalerite-II	+16.5	
FL_{14}-65-06	Core	Sphalerite-II	+16.9	
FL_{14}-95-01	Rim	Pyrite-I	+13.4	
FL_{14}-95-02	Rim	Pyrite-I	+12.8	
FL_{14}-95-03	Rim	Sphalerite-I	+12.5	
FL_{14}-95-04	Core	Sphalerite-I	+23.1	
FL_{14}-13		Galena-II	+11.86	Bulk analysis
FL_{14}-24		Galena-II	+10.49	
FL_{14}-58		Galena-II	+10.04	
FL_{14}-75		Galena-II	+10.66	
FLC-0-1		Sphalerite-II	+15.02	
FLC-0-3		Sphalerite-II	+15.10	
FLC-0-5		Sphalerite-II	+14.21	
FLC-0-8		Sphalerite-I	+14.16	
FLC-0-9		Sphalerite-I	+15.16	
FLC-0-16		Sphalerite-I	+16.43	

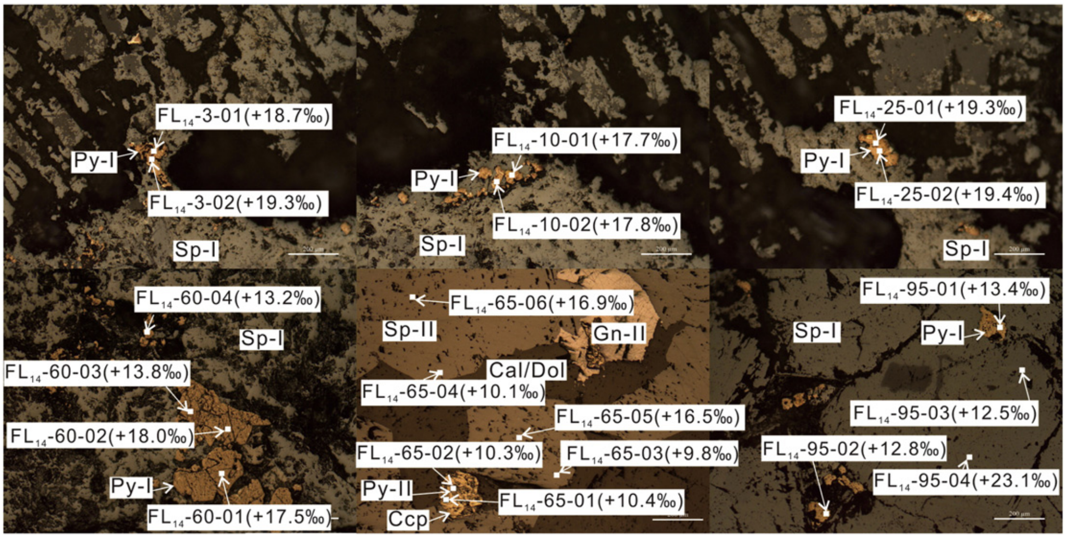

Fig. 11. In situ δ^{34}S values in sphalerite and paragenetic pyrite, showing the in situ δ^{34}S values for sphalerite and pyrite crystals, and their cores and rims.

to −15‰ and +24 to +30‰, respectively (Kump and Arthur, 1999; Hoefs, 2009). Therefore, C—O isotopes can provide an important constraint on the source of ore-forming fluids.

Compared with the above three main reservoirs of CO_2, the calculated $\delta^{13}C_{fluid}$ values (+2.96–+3.40‰) are higher than those of organic matters and the mantle, but are similar to those of carbonate rocks and limestone (Fig. 10). However, the calculated $\delta^{18}O_{fluid}$ values (+7.80–+10.89‰) are lower than those of organic matters, carbonate rocks and limestone (Fig. 10), but are similar to those of mantle or metamorphic fluids (+2–+25‰: Hoefs, 2009). This means that C is mainly derived from limestone, whereas the O isotope signature may be related to water/rock (W/R) interaction between mantle and/or metamorphic fluids and limestone.

Geologically, the mantle-derived basalts of the ELIP and the metamorphic rocks of the Mesoproterozoic Kunyang Group are spatially associated with Pb—Zn deposits in the Fule region (Figs. 1b, 2–3), suggesting that both mantle magmatism and metamorphism have the potential to provide elements and associated fluids to the hydrothermal system, as suggested in other places (Pirajno, 2000; Davidheiser-Kroll et al., 2014). In addition, the occurrence of abundant Cu and Ni sulfide

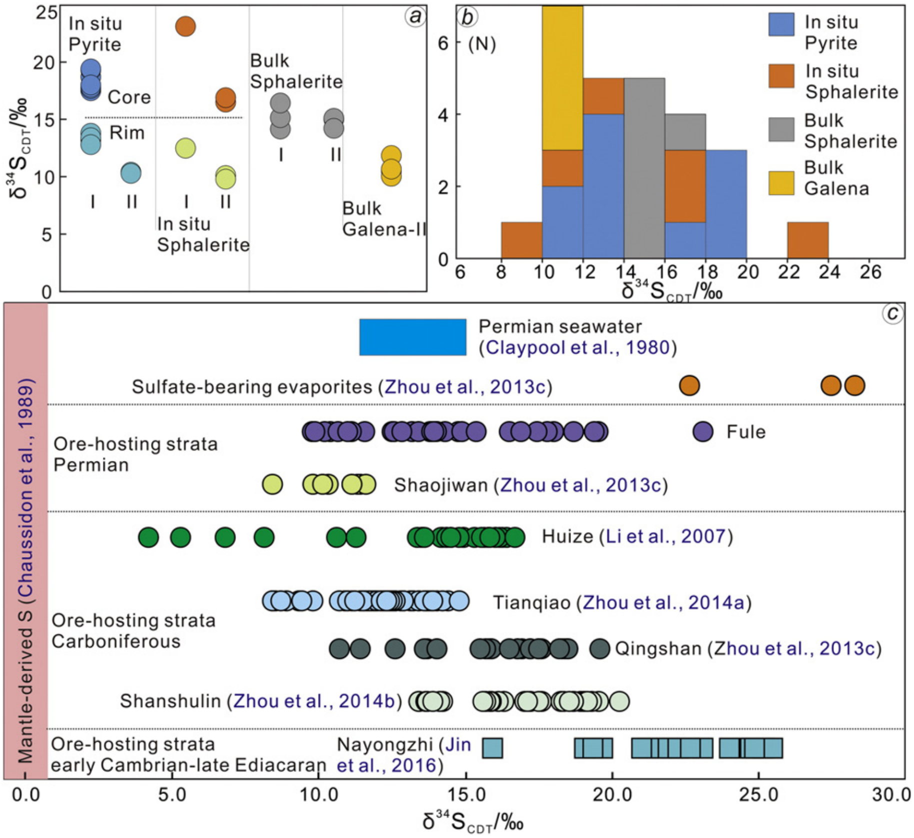

Fig. 12. a: A comparison of in situ and bulk S isotopic compositions for sulfide minerals formed at generations I and II; b: Histogram of in situ and bulk S isotopic data; c: A comparison between mantle-derived S, seawater, evaporates and data from nearby Pb—Zn deposits.

Table 3
In situ Pb isotopic compositions of galena in the Fule deposit.

No.	Mineral	^{206}Pb/^{204}Pb	1 s	^{207}Pb/^{204}Pb	1 s	^{208}Pb/^{204}Pb	1 s
FL_{14}-17-01	Galena-I	18.588	0.003	15.721	0.003	38.678	0.01
FL_{14}-17-02	Galena-I	18.589	0.003	15.724	0.003	38.679	0.007
FL_{14}-17-03	Galena-I	18.585	0.002	15.718	0.002	38.664	0.007
FL_{14}-17-04	Galena-I	18.580	0.002	15.717	0.002	38.664	0.006
FL_{14}-17-05	Galena-I	18.577	0.002	15.713	0.002	38.659	0.008
FL_{14}-17-06	Galena-I	18.581	0.003	15.720	0.003	38.677	0.008
FL_{14}-17-07	Galena-I	18.585	0.002	15.723	0.002	38.682	0.005
FL_{14}-17-08	Galena-I	18.586	0.002	15.721	0.002	38.672	0.006
FL_{14}-25-01	Galena-I	18.582	0.002	15.718	0.002	38.664	0.005
FL_{14}-25-02	Galena-I	18.585	0.002	15.724	0.002	38.681	0.005
FL_{14}-25-03	Galena-I	18.580	0.002	15.719	0.002	38.668	0.005
FL_{14}-25-04	Galena-I	18.582	0.002	15.721	0.002	38.673	0.006
FL_{14}-25-05	Galena-I	18.580	0.002	15.720	0.002	38.682	0.006
FL_{14}-25-06	Galena-I	18.579	0.002	15.716	0.002	38.666	0.007
FL_{14}-25-07	Galena-I	18.588	0.003	15.728	0.003	38.695	0.009
FL_{14}-25-08	Galena-I	18.587	0.002	15.722	0.002	38.683	0.007
FL_{14}-40-01	Galena-I	18.581	0.003	15.715	0.003	38.611	0.008
FL_{14}-40-02	Galena-I	18.584	0.003	15.720	0.003	38.621	0.007
FL_{14}-40-03	Galena-I	18.589	0.002	15.723	0.002	38.637	0.007
FL_{14}-40-04	Galena-I	18.585	0.002	15.719	0.002	38.628	0.006
FL_{14}-40-05	Galena-I	18.573	0.002	15.711	0.002	38.592	0.006
FL_{14}-40-06	Galena-I	18.577	0.003	15.720	0.003	38.615	0.007
FL_{14}-40-07	Galena-I	18.589	0.002	15.721	0.002	38.632	0.006
FL_{14}-40-08	Galena-I	18.596	0.002	15.723	0.003	38.646	0.007
FL_{14}-59-01	Galena-I	18.598	0.002	15.723	0.003	38.648	0.007
FL_{14}-59-02	Galena-I	18.585	0.002	15.711	0.002	38.609	0.007
FL_{14}-59-03	Galena-I	18.589	0.002	15.717	0.002	38.621	0.006
FL_{14}-59-04	Galena-I	18.588	0.002	15.719	0.002	38.620	0.006
FL_{14}-59-05	Galena-I	18.575	0.002	15.718	0.002	38.609	0.005
FL_{14}-59-06	Galena-I	18.572	0.002	15.716	0.002	38.598	0.006
FL_{14}-59-07	Galena-I	18.578	0.003	15.713	0.003	38.597	0.008
FL_{14}-59-08	Galena-I	18.580	0.002	15.712	0.002	38.601	0.006
FL_{14}-75-01	Galena-II	18.606	0.003	15.723	0.003	38.667	0.008
FL_{14}-75-02	Galena-II	18.614	0.002	15.718	0.002	38.718	0.007
FL_{14}-75-03	Galena-II	18.615	0.002	15.717	0.002	38.713	0.006
FL_{14}-75-04	Galena-II	18.610	0.002	15.715	0.002	38.698	0.006
FL_{14}-75-05	Galena-II	18.615	0.002	15.722	0.002	38.715	0.006
FL_{14}-75-06	Galena-II	18.616	0.002	15.727	0.002	38.727	0.006
FL_{14}-75-07	Galena-II	18.609	0.003	15.724	0.003	38.714	0.007
FL_{14}-75-08	Galena-II	18.606	0.002	15.713	0.002	38.689	0.006
FL_{14}-95-01	Galena-II	18.606	0.002	15.712	0.002	38.688	0.006
FL_{14}-95-02	Galena-II	18.617	0.002	15.723	0.002	38.713	0.007
FL_{14}-95-03	Galena-II	18.614	0.002	15.725	0.002	38.714	0.005
FL_{14}-95-04	Galena-II	18.602	0.002	15.722	0.002	38.703	0.005
FL_{14}-95-05	Galena-II	18.598	0.002	15.721	0.002	38.706	0.006
FL_{14}-95-06	Galena-II	18.605	0.002	15.725	0.002	38.706	0.006
FL_{14}-95-07	Galena-II	18.601	0.002	15.716	0.002	38.682	0.007
FL_{14}-95-08	Galena-II	18.595	0.002	15.714	0.002	38.681	0.006

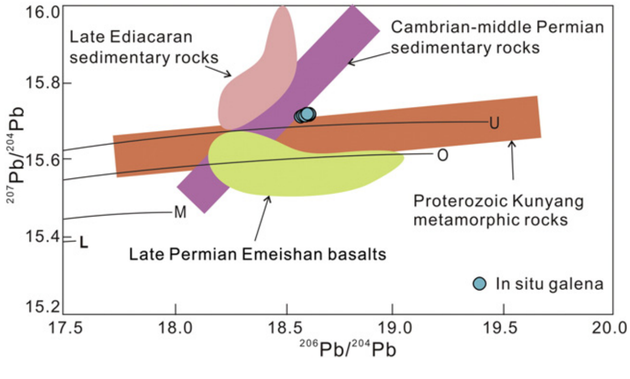

Fig. 13. Plot of ^{207}Pb/^{204}Pb vs. ^{206}Pb/^{204}Pb that shows the field of late Permian Emeishan basalts, late Ediacaran-middle Permian sedimentary rocks and Proterozoic metamorphic rocks, and the Pb evolution curves of U, O, M and L (after Zartman and Doe, 1981); Upper Crust (U), Orogen Belt (O), Mantle (M) and Lower Crust (L). Whole-rock Pb isotopic data are taken from Huang et al. (2004), Li et al. (2007), Yan et al. (2007), Zhou et al. (2013a), J.X. Zhou et al. (2014a) and Bao et al. (2017).

minerals (Figs. 6–8) indicates a genetic relationship between Emeishan magmatism and Pb—Zn mineralization. Furthermore, evidence from in situ Pb isotopic data suggests that the metal Pb was derived from a well-mixed source involving the basalts, sedimentary rocks and metamorphic rocks (see below). Therefore, we propose that the O isotope signature was generated by W/R interaction between mixed (mantle and metamorphic) fluids and limestone.

6.1.2. Constraints from in situ and bulk S isotopes

Primary ore in the Fule deposit is composed of sphalerite, galena, pyrite, and Cu and Ni sulfide minerals, but lacks sulfate minerals (Figs. 4–8). Hence, the $\delta^{34}S$ values of sulfide minerals approximate those of the corresponding fluids, namely $\delta^{34}S_{sulfide} \approx \delta^{34}S_{fluid}$ (Ohmoto, 1972; Seal, 2006). The $\delta^{34}S$ values of sulfide minerals obtained by NanoSIMS in situ analyses compared with bulk techniques range from +9.8 to +23.1‰ (average +15.5‰) and +10.04 to +16.43‰ (average + 13.3‰), respectively (Figs. 11–12), reflecting the enrichment of heavy S isotopes in the hydrothermal fluids. The mean $\delta^{34}S$ value of sulfide minerals is +14.8‰, which approximates that of the ore-forming fluids. Such S isotope signatures differ from mantle-derived S (0 ± 3‰: Chaussidon et al., 1989), and are similar to Permian seawater

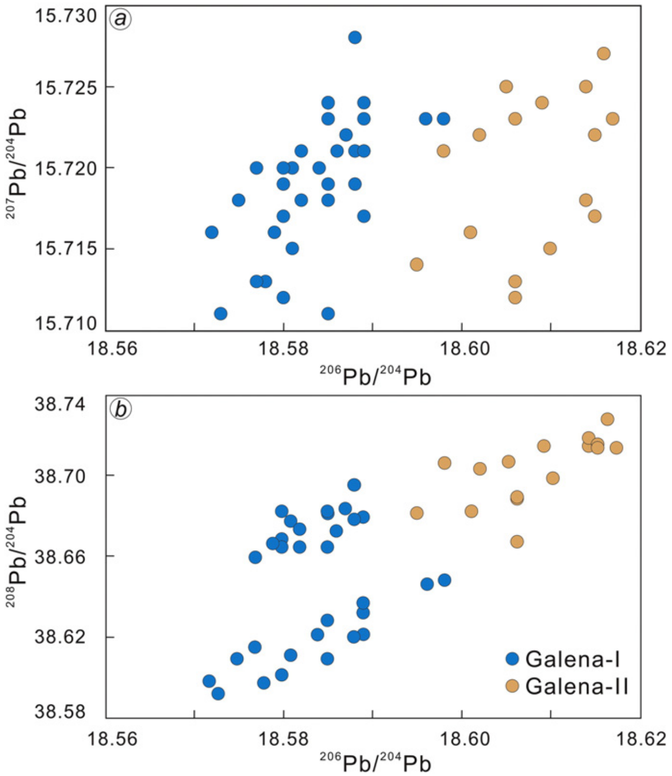

Fig. 14. Plots of $^{207}Pb/^{204}Pb$ vs. $^{206}Pb/^{204}Pb$ (a) and $^{208}Pb/^{204}Pb$ vs. $^{206}Pb/^{204}Pb$ (b) that display the gradually incremental increase in Pb isotopic ratios from galena-I (early phase) to galena-II (late phase).

(+11–+15‰: Claypool et al., 1980; Seal, 2006). Given that the S was completely sourced from Permian seawater, as the thermochemical sulfide reduction (see below) can form up to +15‰ of the $\Delta^{34}S_{sulfate\text{-}sulfide}$ value (Ohmoto et al., 1990; Machel et al., 1995; Worden et al., 1995; Ohmoto and Goldhaber, 1997), so the theoretical $\delta^{34}S_{sulfide}$ value could drop to −4‰. The theoretically predicted $\delta^{34}S_{sulfide}$ values (−7–+15‰) do not match well with the observed $\delta^{34}S$ values (+9.8–+23.1‰). Hence, Permian seawater was not the only S source for the Fule deposit.

Previous studies suggested that the sulfate-bearing evaporites (salt-gypsum rocks) that are common in the late Ediacaran to Triassic marine strata in the region, with $\delta^{34}S$ values ranging from +22 to +28‰ (Fig. 11c; Zhou et al., 2013c), overlap with those of the Ediacaran to Triassic seawater (+10–+35‰: Claypool et al., 1980; Seal, 2006). If the S was totally derived from the above evaporites or seawater, the theoretical $\delta^{34}S_{sulfide}$ values (+7–+28‰ or −5–+35‰) can match reasonably well with the observed $\delta^{34}S$ values (+9.8–+23.1‰). Evidence from S isotopes for the nearby Pb—Zn deposits (Fig. 12c), including the Shaojiwan (hosted in early Permian) (Zhou et al., 2013c), Huize (hosted in early Carboniferous) (Li et al., 2006, 2007), Nayongzhi (hosted in early Cambrian and late Ediacaran) (Jin et al., 2016) and Maozu (hosted in late Ediacaran) (Zhou et al., 2013b), also suggests that the S in the hydrothermal fluids was derived from multiple S reservoirs. Hence, we conclude that the S in the Fule deposit had multiple sources.

Thermochemical sulfate reduction (TSR) and bacterial sulfate reduction (BSR) are two crucial processes for the formation of S^{2-} from SO_4^{2-}, and they are temperature-dependent (Ohmoto et al., 1990; Machel et al., 1995; Hoefs, 2009; Zhou et al., 2013c). TSR occurs at a relatively high temperature (higher than 100–140 °C: Machel et al., 1995; Worden et al., 1995) and can generate a large amount of S^{2-} with relatively stable $\delta^{34}S$ values (Ohmoto et al., 1990; Seal, 2006; Zhou et al., 2013c). BSR occurs at a relatively low temperature (lower than 110 °C: e.g. Jørgenson et al., 1992; Worden et al., 1995; Basuki et al., 2008). As the metallogenic temperature (180–210 °C, based on fluid inclusions in sphalerite-II: Li ZL, unpublished data) is too high for bacteria to survive, hence BSR played an insignificant role in the formation of S^{2-}. In addition, the sulfide ore reserves of the Fule deposit are >10 Mt, which suggests a significant requirement of S^{2-}. This means that TSR has played a crucial role in the formation of S^{2-} from SO_4^2 in the Fule deposit.

The $\delta^{34}S$ values of pyrite-I crystals (rims: +12.8–+13.4‰) are higher than those of paragenetic sphalerite-I crystals (rims: +12.5‰) in sample Fl_{14}-95 (Fig. 11). Similarly, in sample Fl_{14}-65 (Fig. 11), pyrite-II crystals have $\delta^{34}S$ values (rims: +10.3–+10.4‰) higher than those of paragenetic sphalerite-II crystals (rims: +9.8–+10.1‰). Such S isotope signatures suggest that the fractionation of S isotopes between pyrite and paragenetic sphalerite reached equilibrium (Ohmoto, 1972; Seal, 2006). In addition, sphalerite-II has $\delta^{34}S$ values (+14.21–+15.10‰) higher than those of galena-II (+10.04–+11.86‰) (Fig. 12a), which indicates that S isotope fractionation between sphalerite and galena had also reached equilibrium (Seal, 2006; Hoefs, 2009). Hence, equilibrium fractionation played an important role in the variation of $\delta^{34}S$ values for the sulfide minerals in the Fule deposit. On the other hand, the $\delta^{34}S$ values decrease gradually from core to rim in both sphalerite and pyrite crystals (Fig. 11), which suggests that other factors may have controlled the S isotope signatures, such as changes in the physico-chemical conditions (T, pH, f_{O_2}, f_S, etc.), Rayleigh fractionation, or mixing of multiple S reservoirs (Ohmoto, 1972; Hoefs, 2009). Previous studies suggested that physical and chemical conditions are crucial factors that can cause large variations in S isotopes (Seal, 2006; Hoefs, 2009). However, the circulating process (dissolution and re-precipitation) of local carbonate rocks that was caused by water/rock (W/R) interaction (O'Neil et al., 1969; Zheng and Hoefs, 1993; Warren, 2000) can help keep a metastable metallogenic environment (see below). Hence, changes in physical-chemical conditions can be ruled out. In contrast, as a consequence of dynamic fractionation, heavy S isotopes are expected to be more enriched in the cores of sulfide minerals than their rims (Figs. 11–12) during precipitation, due to the fact that light S isotopes are more enriched in the gas phase (H_2S) (Seal, 2006; Zhou et al., 2013c). Alternatively, a mixing process of multiple reservoirs and associated fluids can cause distinct variation of S isotopes (Basuki et al., 2008; Zhou et al., 2013c), and our isotopic data imply that multiple reservoirs were involved (Figs. 11–12), providing the S source for the formation of the Fule sulfide ore. Therefore, both equilibrium and dynamic fractionation of S isotopes occurred during sulfide precipitation.

6.1.3. Evidence from in situ Pb isotopes

The extremely low U and Th contents in sulfide minerals (Carr et al., 1995; Muchez et al., 2005; Zhou et al., 2013a; Pass et al., 2014) enables us to use the Pb isotopic ratios of galena formed at different paragenetic stages in the Fule deposit to investigate the nature of the hydrothermal fluids. Uniform in situ Pb isotopic ratios of galena suggest a single or a well-mixed source of Pb (Fig. 13). The Pb isotopic data plot above the Pb evolution curve of the average upper continental crust in the diagram of $^{207}Pb/^{204}Pb$ vs. $^{206}Pb/^{204}Pb$ (Fig. 13) (Zartman and Doe, 1981).

Previous studies suggested that there are three potential metal sources in the SYG province, namely the late Permian Emeishan basalts, ore-hosting late Ediacaran to middle Permian sedimentary rocks and Meso- to Neo-proterozoic metamorphic rocks (Zheng and Wang, 1991; Zhou et al., 2001, 2013a; Huang et al., 2004; Li et al., 2007, 2015, 2016; Zhang et al., 2015; Jin et al., 2016; Zhu et al., 2017). Compared with the basalts, sedimentary rocks and basement rocks, galena has Pb isotopic ratios that differ from all of them in the diagram of $^{207}Pb/^{204}Pb$ vs. $^{206}Pb/^{204}Pb$ (Fig. 13). This means that there was not a single source for the Pb. In addition, galena displays higher $^{207}Pb/^{204}Pb$ than those of the basalts and basement rocks at a given $^{206}Pb/^{204}Pb$ ratio (Fig. 13), but both the galena and the basalts, sedimentary rocks and basement rocks have the same $^{206}Pb/^{204}Pb$ ratio at a given $^{206}Pb/^{204}Pb$ ratio (Fig. 13). It should be noted that many of the ELIP basalts show evidence of crustal contamination and that it is possible the contamination originated from carbonate rocks (possibly their fluids) (Xu et al., 2001; Pirajno, 2013; Shellnutt, 2014). Hence, we cannot rule out contribution from the ELIP basalts (6–323 μg/g Cu, 66–156 μg/g Zn and 3–30 μg/g Pb: Huang et al., 2004; Xu et al., 2001, 2007) and we consider a well-mixed metal source is a reasonable postulate (Fig. 13).

There is a gradual increase in the $^{206}Pb/^{204}Pb$ and $^{208}Pb/^{204}Pb$ ratios from galena-I to galena-II (Fig. 14a–b), which can be explained by: (a) a high $^{206}Pb/^{204}Pb$ and $^{208}Pb/^{204}Pb$-enriched source provided more Pb for galena-II than galena-I, or (b) galena-I had lower ^{238}U and ^{232}Th contents than galena-II. Because of the low U and Th contents in galena, and the lack of any distinct difference between the two generations of galena (Zhou et al., 2011; Ye et al., 2011 and unpublished data), so a highly radiogenic Pb-enriched source (such as basalts or basements), which may have provided more Pb to the hydrothermal fluids in the late phase is possible. This explanation is further supported by the occurrence of abundant Cu and Ni sulfide minerals in the late phase (Figs. 6–8).

6.2. Precipitation mechanisms of hydrothermal minerals

6.2.1. Mechanisms of calcite precipitation

As the solubility of calcite decreases with increase in temperature, so cooling of the fluid itself could not cause calcite precipitation (Zheng, 1990; Barnes, 1997; Hoefs, 2009). There are three main processes that can lead to calcite precipitation in an open hydrothermal system, i.e. fluid mixing, water/rock (W/R) interaction and CO_2 degassing (Zheng and Hoefs, 1993; Huang et al., 2010; Du et al., 2017). Our C isotopic data suggest that C is sourced mainly from the limestone (Fig. 10). This means that the process of fluid mixing played an insignificant role in calcite precipitation. As a consequence of W/R interaction, the circulating process between dissolution and re-precipitation in carbonate rocks can cause calcite precipitation, at least locally (Warren, 2000). Moreover, such circulating processes of precipitation → dissolution → re-precipitation can generate metastable conditions that are beneficial to the continuous formation of sulfide ore (Zhou et al., 2018). In addition, the C—O isotopic evolution curve of W/R interaction between fluids (initial $\delta^{13}C_{fluid} = +2‰$, $\delta^{18}O_{fluid} = +6‰$) and limestone (Fig. 15) was simulated, using the fractionation factor and equation of C—O isotopes (O'Neil et al., 1969; Zheng and Hoefs, 1993). The simulation results suggest that our C—O isotopic data match well with the evolution curves of both HCO_3^- and H_2CO_3 (Fig. 15) as the dominant C species (Zheng and Hoefs, 1993). Similarly, the C—O isotopic evolution curve of CO_2 degassing (with 0.1, 0.2, 0.3 and 0.4 mol fraction of total C and O; initial $\delta^{13}C_{fluid} = +2‰$, $\delta^{18}O_{fluid} = +6‰$) was also simulated (Fig. 16a–b). The results show that our C—O isotopic data still match well with the evolution curve of both H_2CO_3 (Fig. 16a) and HCO_3^- (Fig. 16b) as the dominant C species. Hence, calcite precipitation was controlled by both W/R interaction and CO_2 degassing.

6.2.2. Mechanisms of sulfide precipitation

Previous studies suggested that there are three main models (reduced S, local sulfate reduction, and mixing of metal and reduced S) that can account for sulfide precipitation in hydrothermal systems (Anderson, 1975; Corbella et al., 2004; Leach et al., 2005). The reduced S model requires metal and reduced S to be transported together to the depositional site; the local sulfate reduction model calls upon increasing the concentration of reduced S at the depositional site through sulfate reduction; and the mixing of metal and reduced S demands a metal-rich, but reduced S-poor brine, mixed with a fluid rich in hydrogen sulfide at the depositional site (Heijlen et al., 2003; Leach et al., 2005). Our S isotopic data suggest that S was derived from multiple reservoirs and TSR played a dominant role in the formation of S^{2-} from SO_4^{2-} (Figs. 11–12). However, our Pb isotopic data indicate that a

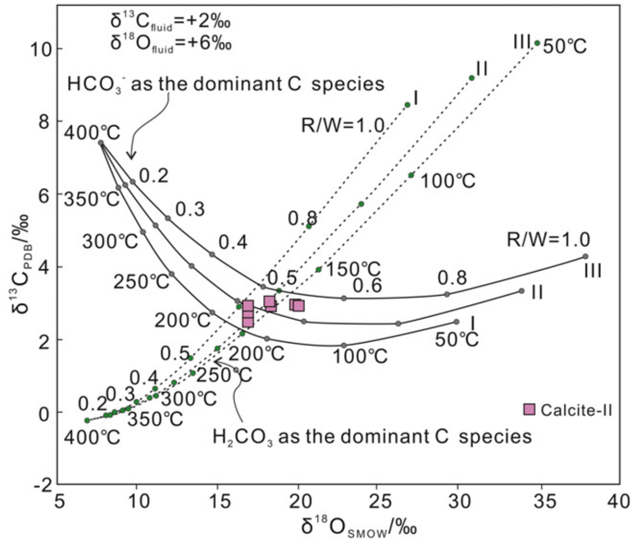

Fig. 15. Diagram of $\delta^{13}C$ vs. $\delta^{18}O$ for calcite precipitated by W/R interaction with different R/W ratios and temperatures (400–50 °C) for either HCO_3^- or H_2CO_3 as the dominant C species (after Zheng and Hoefs, 1993), showing the position of calcite-II. Initial fluids: $\delta^{13}C = +2‰$, $\delta^{18}O = +6‰$. $\Delta = \delta^{i}_{rock} - \delta^{f}_{rock}$; I: $\Delta^{13}C = +0.2‰$, $\Delta^{18}O = +2‰$; II: $\Delta^{13}C = +1‰$, $\Delta^{18}O = +6‰$; III: $\Delta^{13}C = +2‰$, $\Delta^{18}O = +10‰$.

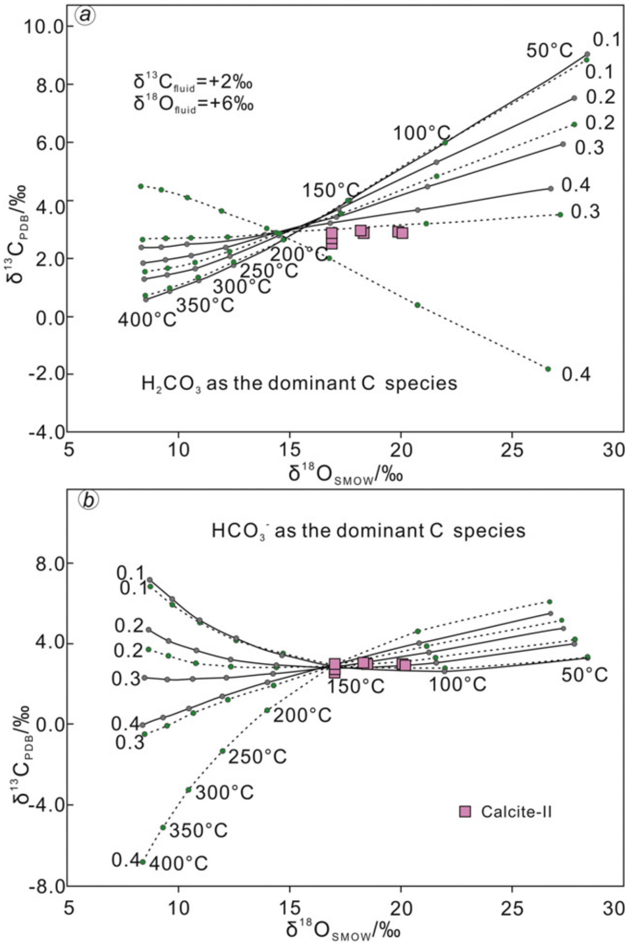

Fig. 16. Plots of $\delta^{13}C$ vs. $\delta^{18}O$ for calcite precipitated by CO_2 degassing with H_2CO_3 (a) or HCO_3^- (b) as the dominant C species (after Zheng, 1990), showing the position of calcite-II. The batch (solid line) and Rayleigh (dashed line) degassing precipitation models change with temperature (400–50 °C) and mol fraction of C in the degassed CO_2 (0.1 to 0.4) (after Zheng, 1990). The initial $\delta^{13}C_{fluid}$ and $\delta^{18}O_{fluid}$ values were taken as +2‰ and +6‰, respectively.

well-mixed source of the basalts, sedimentary rocks and basement rocks provided the main metal source (Figs. 13–14). As the normal SO_4^{2-}-bearing basin brines are of low temperature (usually <100 °C) (Corbella et al., 2004; Leach et al., 2005), which is lower than the required temperature for activating TSR, so the aforementioned three models cannot reasonably explain the formation of sulfide ore in the Fule deposit. Therefore, an alternative model is proposed here, namely fluid mixing caused by TSR, which then resulted in sulfide precipitation.

6.3. Possible mineralizing age and related geological events

In the Fule mining area, the ore-bearing strata are the middle Permian Yangxin Formation (Figs. 2–3), which implies that the ore formation time was not older than middle Permian age. In addition, the evidence from mineralogy (Cu and Ni sulfide minerals) (Figs. 6g, i, k, m, r–t and 7g–h, j, l–s), and O (Fig. 10) and Pb isotopes (Figs. 13–14) reveals a genetic association with Emeishan magmatism. This reflects that mineralization may have occurred at the same time as the ELIP. The most reliable radiometric dates indicate generation of the ELIP at 263–259 Ma (Xu et al., 2001; Zhou et al., 2002; Ali et al., 2005; Shellnutt et al., 2012). On the other hand, sulfide ore in the Fule deposit occurs as stratiform to lentiform shapes or as veins along the bedding-planes, locally associated with the Mile-Shizong-Shuicheng regional fault system and the Faben anticline (Figs. 1b, 2–3). These structures were activated during the Indosinian Orogeny (Lu et al., 2015), which suggests that the Fule deposit was most likely formed during the Indosinian period (257–200 Ma: Carter et al., 2001; Enkelmann et al., 2007; Reid et al., 2007; Lepvrier et al., 2008; Pullen et al., 2008). Furthermore, according to the Pb model ages, Si et al. (2006) considered that the Fule deposit was probably formed during late Triassic to early Jurassic (~225–198 Ma). This age broadly matches the dates of the nearby Pb—Zn deposits (245–192 Ma) (Guan and Li, 1999; Li et al., 2007; Lin et al., 2010; Mao et al., 2012; Zhou et al., 2013a, 2013b, 2015; Zhang et al., 2015), native Cu deposits (230–225 Ma) (Zhu et al., 2007) and Carlin-like Au deposits (235–204 Ma) (Chen et al., 2015). Hence, the Fule and nearby deposits were formed between 250 and 200 Ma, and were most likely related to the ELIP and the Indosinian Orogeny that occurred after eruption of the Emeishan basalts.

6.4. Ore genesis

Sulfide ore in the Fule deposit has a spatial association with the Emeishan basalts (Figs. 1b, 2–3), which led some researchers to classify it as a distal magmatic-hydrothermal type (Xie, 1963). Other geological evidence linking mineralization to Emeishan magmatism includes the occurrence of hidden Pb—Zn veins in the basalts at Xuanwei County, NE Yunnan Province (Liu and Lin, 1999). On the other hand, sulfide ore in the Fule deposit occurs in stratiform to lentiform shapes or veins (Figs. 3–4) that are clearly stratabound. This led other researchers to classify it as a Sedimentary Exhalative-type (SEDEX) or a stratabound-type of deposit (Si et al., 2006). However, the Fule sulfide ore is hosted by middle Permian carbonate rocks, which are different from clastic rocks that host sulfide ore of SEDEX-type (Leach et al., 2005). In addition, based on the evidence of Cd isotopes, the Fule deposit was considered to be a Mississippi Valley-type (MVT) deposit (Zhu et al., 2017). Traditionally, typical MVT deposits are related to basin fluids that are characterized by low temperatures (50–200 °C) and high salinities (10–30 wt% NaCl equiv.) and have no genetic association

Table 4
A comparison between the Fule, Huize and typical MVT deposits.

Characteristics	Huize (typical SYG-type)	MVT	Fule
Grade	Pb + Zn: 25–35 wt%, Zn/(Zn + Pb): 0.9±	Pb + Zn: av. <10 wt%, Zn/(Zn + Pb): 0.8±	Pb + Zn: av. 15–20 wt%, Zn/(Zn + Pb): 0.9±
Tonnage	Pb + Zn metal reserves: single ore body ~1 Mt, total > 7 Mt	Pb + Zn metal reserves: single ore body <1 Mt	Pb + Zn metal reserves: single ore body ~0.5 Mt, total > 1 Mt
Acreage	The SYG province covers 170, 000 km^2	Hundreds of square kilometers	The SYG province covers 170, 000 km^2
Host rocks	Early Carboniferous coarse-grained dolostone	Cambrian to Carboniferous carbonate rocks	Middle Permian dolostone
Depth of mineralization	>2000 m	<1500 m	<400 m
Tectonic setting	Western Yangtze Block, controlled by NE reverse fault-fold tectonic system	Typically located within extensional zones inboard of orogenic belts	Western Yangtze Block, controlled by NE reverse fault-fold tectonic system
Relation with magmatic activity	Genetically associated with late Permian Emeishan basalts	Generally has no genetic association with magmatic activity	Genetically associated with late Permian Emeishan basalts
Ore-controlled factors	Controlled by thrust fault-fold structure and lithology	Mainly controlled by structure and lithology	Controlled by fault-fold structure and lithology
Age	~225 Ma	From Proterozoic to Cretaceous	250–200 Ma
Ore texture and structure	Mainly exhibiting massive structures, and fine-, medium- and coarse-grained textures	Exhibiting disseminated, fine granular, branched, colloidal and massive structures and colloidal, skeleton coarse-crystalline textures	Mainly exhibiting massive structures, and fine-, medium- and coarse-grained textures
Mineral compositions	Sphalerite, galena, pyrite and calcite	Sphalerite, galena, pyrite, barite, fluorite, calcite and dolomite.	Sphalerite, galena, pyrite, chalcopyrite, tetrahedrite, millerite, polydymite, pentlandite, calcite and dolomite
Fluid inclusions	<10 wt% NaCl equiv.; Cl^--Na^+-Ca^{2+}-Mg^{2+}-SO_4^{2-}; 150–300 °C	10–30 wt% NaCl equiv.; Cl^--Na^+-Ca^{2+}-K^+-Mg^{2+}; 50–200 °C	4–10 wt% NaCl equiv.; Cl^--Na^+-Ca^{2+}-Mg^{2+}-SO_4^{2-}; 120–260 °C
Associated metals	Ag, Cu, Ge, Ga, Cd and In	Ag	Ag, Cu, Ni, Cd, Ge, Ga and In
O isotopes	Generated from W/R interaction between mantle/metamorphic fluids and carbonate rocks	Sourced from carbonate rocks	Generated from W/R interaction between/metamorphic fluids and carbonate rocks
S isotopes	+11–+17‰, sourced from multiple S reservoirs	+10–+25‰, sourced from evaporates within sedimentary strata	+9–+23‰, sourced from multiple S reservoirs
Pb isotopes	Normal and uniform Pb isotopes, sourced from a well-mixed source	Complicated Pb isotopic ratios and regional zonation	Normal and uniform Pb isotopes, sourced from a well-mixed source
Precipitation of sulfide	Fluid mixing + sulfate reduction	Reduced S, local sulfate reduction, or metal and reduced S-mixing	Fluid mixing + sulfate reduction
Tectonic setting	Changed from compression to extension	Extensional basin	Changed from compression to extension
References	Zhou et al., 2001; Li et al., 2007; Huang et al., 2010	Leach et al., 2005, 2010	Zhu et al., 2017; this paper

with magmatic activity (Leach et al., 2005, 2010). However, the study of fluid inclusions in sphalerite suggests that the ore-forming fluids in the Fule deposit are characterized by low-medium temperatures (120–260 °C) and low salinities (4–10 wt% NaCl equiv.) (Si et al., 2006; Li ZL, unpublished data). In addition, the occurrence of abundant Cu and Ni sulfide minerals (Figs. 6g, i, k, m, r–t and 7g–h, j, l–s), and the evidence of O (Fig. 10) and Pb isotopes (Figs. 13–14) imply that the formation of sulfide ore in the Fule deposit was associated with the ELIP. Furthermore, these features are similar to those of the unique SYG-type Huize Pb-Zn deposit (Zhou et al., 2001; Huang et al., 2004; Li et al., 2007) (Table 4). Moreover, the sulfide ore in the Fule deposit is of higher grades (up to 60 wt% Zn + Pb, av. 15–20 wt%) than those of MVT deposits (usually <10. Wt% Zn + Pb). Hence, we propose that the Fule deposit is not a typical MVT deposit and represents a new unique SYG-type of deposit that is between MVT and magmatic hydrothermal deposits.

6.5. Ore formation process and relationship with the ELIP

Pirajno (2000) established indirect links with sediment-hosted deposits (such as MVT and SEDEX-type) and mantle plumes. The thermal simulation indicates that the basalts of the EILP begin to release metal-bearing fluids at ~5–10 Ma after it erupting and this process can last over ~50 Ma (Xu et al., 2014). On the other hand, if we consider that the Pb—Zn deposits in the ELIP formed as a consequence of Indosinian tectonism (~257–200 Ma: Carter et al., 2001; Lepvrier et al., 2004; Enkelmann et al., 2007; Reid et al., 2007; Pullen et al., 2008), then it makes sense that magmatic fluids related to the Emeishan event could pass through the carbonate rocks and be involved in the mineralization. Furthermore, metal-bearing fluids (including thermal flux and volatiles) generated by Emeishan magmatism have been shown to be involved in the formation of the Fule deposit, as evidenced by field data (Figs. 1–8), fluids compositions (Figs. 10, 12, 15–16), and in situ S (Figs. 9, 11–12) and Pb (Figs. 13–14) isotopes. In addition, hydrothermal fluids responsible for carbonate-hosted base metal deposits in the Irish Pb—Zn ore district was considered to be driven by mantle heat (Davidheiser-Kroll et al., 2014). Hence, sulfide ore in the Fule deposit has a genetic relationship with Emeishan magmatism.

Between 263 and 259 Ma, during the eruption of the Emeishan basalts (Shellnutt, 2014), fluids were provided (thermal flux + volatiles) and there was an elevated background geothermal gradient, both of which facilitated and enhanced the mobilization and extraction of ore-forming elements from Proterozoic metamorphic rocks in the basement

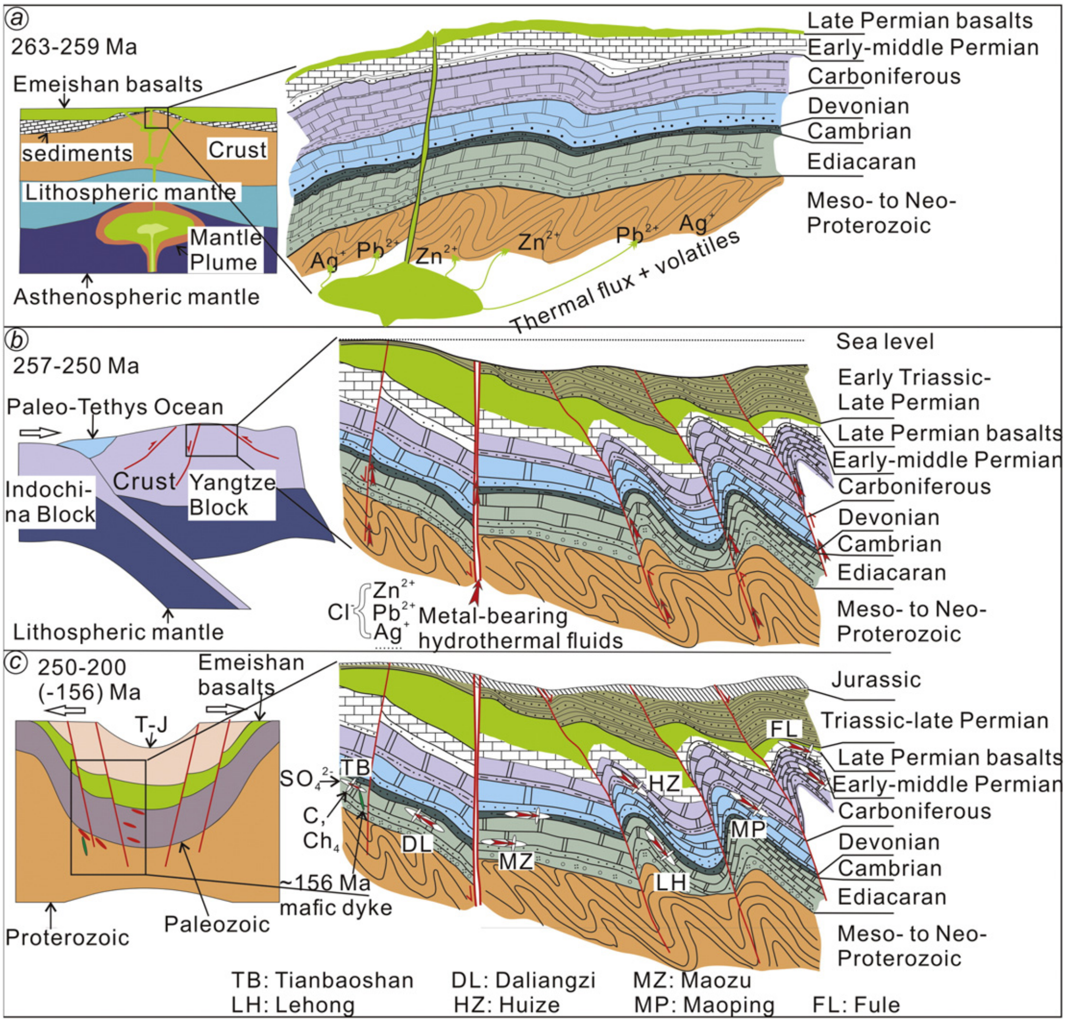

Fig. 17. A sketch of the metallogenic model favoured for the carbonate-hosted Pb—Zn deposits in the ELIP; a: 263–259 Ma, the eruption of the Emeishan basalts (Shellnutt, 2014) provided fluids and elevated background geothermal gradient, which facilitated and enhanced the mobilization and extraction of ore-forming elements from Proterozoic metamorphic rocks and Paleozoic sedimentary rocks; b: 257–250 Ma, metal-bearing mantle and metamorphic fluids were driven upward along regional faults during the early Indosinian Orogeny (Carter et al., 2001; Reid et al., 2007; Hu et al., 2017); c: 250–200 (—156 Ma), the ore-forming fluids were released into structural units when the overall tectonic regime changed from compression to extension between 250 and 200 Ma (Carter et al., 2001; Lepvrier et al., 2008; Zhou et al., 2013b), where they were trapped by the evaporitic salt and sedimentary organic-bearing units within the platform carbonate sequence at structurally-controlled depositional sites. This process resulted in the formation of S^{2-} from multiple S reservoirs via TSR and the extraction of some metals from ore-hosting rocks through W/R interaction, which then caused the precipitation of hydrothermal minerals.

and Paleozoic sedimentary rocks (Fig. 17a). Following eruption of the Emeishan basalts, these metal-bearing mixed (mantle and metamorphic) fluids (initial $\delta^{13}C_{fluid} = +2‰$, $\delta^{18}O_{fluid} = +6‰$) were driven upward along regional faults (including the Mile-Shizong-Shuicheng fault and its subsidiaries; Fig. 1a) during the early Indosinian Orogeny (257–250 Ma) (Fig. 17b). These fluids were then released into structural units (such as the Faben anticline) when the overall tectonic regime changed from compression to extension between 250 and 200 Ma (Fig. 17c) (Carter et al., 2001; Reid et al., 2007; Lepvrier et al., 2008; Lu et al., 2015; Qiu et al., 2016). The fluids were then trapped by evaporitic salt and sedimentary organic-bearing units within the platform carbonate sequences at the structurally-controlled depositional sites (Fig. 17c). This process resulted in the formation of S^{2-} from multiple S reservoirs via TSR and the extraction of some metals from ore-hosting strata through W/R interaction (as evidenced by C—O—S and Pb isotopes), and then resulted in the precipitation of hydrothermal minerals (Fig. 17c). Importantly during ore formation, the Emeishan basalts also acted as an impermeable and protective layer (Figs. 1b, 2–3, 17) and even acted as ore-hosting rocks, which enabled the massive accumulation of Cu, Pb—Zn, and even Au ores in the western Yangtze Block (Fig. 1b).

7. Conclusions

(a) Bulk C—O isotopic data suggest that the source of C in the Fule Pb—Zn deposit was limestone, whereas the O isotope signature is related to W/R interaction between mixed (mantle and metamorphic) fluids and limestone. W/R interaction and CO_2 degassing are two crucial processes for calcite precipitation.

(b) Both in situ and bulk S isotopic data indicate a mixed S source from multiple reservoirs and that TSR played a crucial role in the formation of S^{2-}. Both equilibrium and dynamic fractionation controlled the variation in S isotopes.

(c) In situ Pb isotopic data imply a well-mixed Pb source that includes basalts, sedimentary rocks and Proterozoic basement rocks.

(d) The Fule Pb—Zn deposit thus represents a new unique SYG-type of deposit that is between MVT and magmatic hydrothermal deposits.

Acknowledgements

This research was financially supported by the National Key Research and Development Project of China (2017YFC0602502), the Key Program of National Natural Science Foundation of China (41430315), the National Basic Research Program of China (2014CB440905), and the Visiting Scholar Project of China Scholarship Council to Jia-Xi Zhou (201604910455). We thank Profs. Lin Ye (IG CAS) and Mei-Fu Zhou (University of Hong Kong) for fruitful discussions. We thank Prof. Franco Pirajno (Associate Editor), Prof. Greg Shellnutt and anonymous reviewers for their constructive suggestions and comments.

References

Ali, J.R., Thompson, G.M., Zhou, M.F., Song, X.Y., 2005. Emeishan large igneous province, SW China. Lithos 79, 475–489.

Anderson, G.M., 1975. Precipitation of Mississippi Valley-type ores. Economic Geology 70, 937–942.

Anderson, G.M., Macqueen, R.W., 1982. Ore deposit models-6. Mississippi Valley-type lead-zinc deposits. Geoscience Canada 9, 108–117.

Bai, J., Huang, Z., Zhu, D., Yan, Z., Zhou, J., 2013. Isotopic compositions of sulfur in the Jinshachang lead-zinc deposit, Yunnan, China, and its implication on the formation of sulfur-bearing minerals. Acta Geologica Sinica (English Edition) 87, 1355–1369.

Bao, Z., Yuan, W., Yuan, H., Liu, X., Chen, K., Zong, C., 2016. Non-matrix-matched determination of lead isotope ratios in ancient bronze artifacts by femtosecond laser ablation multi-collector inductively coupled plasma mass spectrometry. International Journal of Mass Spectrometry 402, 12–19.

Bao, Z., Li, Q., Wang, C.Y., 2017. Metal source of giant Huize Zn-Pb deposit in SW China: new constraints from in situ Pb isotopic compositions of galena. Ore Geology Reviews https://doi.org/10.1016/j.oregeorev.2017.08.019.

Barker, S.L., Hickey, K.A., Cline, J.S., Dipple, G.M., Kilburn, M.R., Vaughan, J.R., Longo, A.A., 2009. Uncloaking invisible gold: use of nanoSIMS to evaluate gold, trace elements, and sulfur isotopes in pyrite from Carlin-type gold deposits. Economic Geology 104, 897–904.

Barnes, H.L., 1997. Geochemistry of Hydrothermal Ore Deposits. vol. 1. John Wiley & Sons.

Basuki, N.I., Taylor, B.E., Spooner, E.T.C., 2008. Sulfur isotope evidence for thermochemical reduction of dissolved sulfate in Mississippi valley type zinc-lead mineralization, Bongara area, northern Peru. Economic Geology 103, 183–799.

Bottinga, Y., 1968. Calculation of fractionation factors for carbon and oxygen isotopic exchange in the system calcite-carbon dioxide-water. The Journal of Physical Chemistry 72, 800–808.

Carr, G.R., Dean, J.A., Suppel, D.W., Heithersay, P.S., 1995. Precise lead isotope fingerprinting of hydrothermal activity associated with Ordovician to Carboniferous metallogenic events in the Lachlan fold belt of New South Wales. Economic Geology 90, 1467–1505.

Carter, A., Roques, D., Bristow, C., Kinny, P., 2001. Understanding Mesozoic accretion in Southeast Asia: significance of Triassic thermotectonism (Indosinian Orogeny) in Vietnam. Geology 29, 211–214.

Chaussidon, M., Albarède, F., Sheppard, S.M.F., 1989. Sulphur isotope variations in the mantle from ion microprobe analyses of micro-sulphide inclusions. Earth and Planetary Science Letters 92, 144–156.

Chen, K.Y., Yuan, H.L., Bao, Z.A., Zong, C.L., Dai, M.N., 2014. Precise and accurate in situ determination of lead isotope ratios in NIST, USGS, MPI-DING and CGSG glass reference materials using femtosecond laser ablation MC-ICP-MS. Geostandards and Geoanalytical Research 38, 5–21.

Chen, M., Mao, J., Li, C., Zhang, Z., Dang, Y., 2015. Re-Os isochron ages for arsenopyrite from Carlin-like gold deposits in the Yunnan-Guizhou-Guangxi “golden triangle”, southwestern China. Ore Geology Reviews 64, 316–327.

Claypool, G.E., Holser, W.T., Kaplan, I.R., Sakai, H., Zak, I., 1980. The age curves of sulfur and oxygen isotopes in marine sulfate and their mutual interpretation. Chemical Geology 28, 199–260.

Corbella, M., Ayora, C., Cardellach, E., 2004. Hydrothermal mixing, carbonate dissolution and sulfide precipitation in Mississippi Valley-type deposits. Mineralium Deposita 39, 344–357.

Davidheiser-Kroll, B., Stuart, F.M., Boyce, A.J., 2014. Mantle heat drives hydrothermal fluids responsible for carbonate-hosted base metal deposits: evidence from $^{3}He/^{4}He$ of ore fluids in the Irish Pb-Zn ore district. Mineralium Deposita 49, 547–553.

Demény, A., Ahijado, A., Casillas, R., Vennemann, T.W., 1998. Crustal contamination and fluid/rock interaction in the carbonatites of Fuerteventura (Canary Islands, Spain): a C, O, H isotope study. Lithos 44, 101–115.

Deng, J., Wang, C., Bagas, L., Selvaraja, V., Jeon, H., Wu, B., Yang, L., 2017. Insights into ore genesis of the Jinding Zn–Pb deposit, Yunnan Province, China: evidence from Zn and in-situ S isotopes. Ore Geology Reviews https://doi.org/10.1016/j.oregeorev.2016.10.036.

Du, L.J., Li, B., Huang, Z.L., Zhou, J.X., Zou, G.F., Yan, Z.F., 2017. Carbon-oxygen isotopic geochemistry of the Yangla Cu skarn deposit, SW China: implications for the source and evolution of hydrothermal fluids. Ore Geology Reviews 88, 809–821.

Enkelmann, E., Weislogel, A., Ratschbacher, L., Eide, E., Renno, A., Wooden, J., 2007. How was the Triassic Songpan-Ganzi basin filled? A provenance study. Tectonics 26. https://doi.org/10.1029/2006TC002078.

Gao, S., Yang, J., Zhou, L., Li, M., Hu, Z.C., Guo, J.L., Yuan, H.L., Gong, H.J., Xiao, G.Q., Wei, J.Q., 2011. Age and growth of the Archean Kongling terrain, South China, with emphasis on 3.3 Ga granitoid gneisses. American Journal of Science 311, 153–182.

Guan, S.P., Li, Z.X., 1999. Pb and S isotope study of carbonate-hosted Pb-Zn deposits at the eastern margin of the Kangdian axis. Geology Geochemistry 27, 45–54 (in Chinese with English abstract).

Heijlen, W., Muchez, P., Banks, D.A., Schneider, J., Kucha, H., Keppens, E., 2003. Carbonate-hosted Zn-Pb deposits in Upper SiJesia, Poland: origin and evolution of mineralizing fluids and constraints on genetic models. Economic Geology 98, 911–932.

Hoefs, J., 2009. Stable Isotope Geochemistry. sixth edition. Springer-Verlag, Berlin Heidelberg https://doi.org/10.1007/978-3-540-70708-0.

Hu, R.Z., Zhou, M.F., 2012. Multiple Mesozoic mineralization events in South China-an introduction to the thematic issue. Mineralium Deposita 47, 579–588.

Hu, R., Fu, S., Huang, Y., Zhou, M., Fu, S., Zhao, C., Wang, Y., Bi, X., Xiao, J., 2017. The giant South China Mesozoic low-temperature metallogenic domain: reviews and a new geodynamic model. Journal of Asian Earth Sciences 137, 9–34.

Huang, Z.L., Chen, J., Han, R.S., Li, W.B., Liu, C.Q., Zhang, Z.L., Ma, D.Y., Gao, D.R., Yang, H.L., 2004. Geochemistry and Ore Genesis of the Huize Giant Pb-Zn Deposit in Yunnan Province, China: Discussion on the Relationship Between the Emeishan Flood Basalts and Pb-Zn Mineralization. Geological Publishing House, Beijing, pp. 1–214 (in Chinese).

Huang, Z., Li, X., Zhou, M., Li, W., Jin, Z., 2010. REE and C-O isotopic geochemistry of calcites from the word-class Huize Pb-Zn deposits, Yunnan, China: implication for the ore genesis. Acta Geologica Sinica (English edition) 84, 597–613.

Ikehata, K., Notsu, K., Hirata, T., 2008. In situ determination of Cu isotope ratios in copper-rich materials by NIR femtosecond LA-MC-ICP-MS. Journal of Analytical Atomic Spectrometry 23, 1003–1008.

Jian, P., Li, D.Y., Kröner, A., Zhang, Q., Wang, Y.Z., Sun, X.M., Zhang, W., 2009. Devonian to Permian plate tectonic cycle of the Paleo-Tethys Orogen in southwest China (II): insights from zircon ages of ophiolites, arc/back-arc assemblages and within-plate igneous rocks and generation of the Emeishan CFB province. Lithos 113, 767–784.

Jin, Z.G., 2008. The Ore-control Factors, Ore-forming Regularity and Ore Forecasting of Pb-Zn Deposits in NW Guizhou Province. Engine Industry Press, Beijing, pp. 1–105 (in Chinese).

Jin, Z.G., Zhou, J.X., Huang, Z.L., Ye, L., Luo, K., Gao, J.G., Chen, X.L., Wang, B., Peng, S., 2016. Ore genesis of the Nayongzhi Pb-Zn deposit, Puding city, Guizhou Province, China: evidences from S and in situ Pb isotopes. Acta Petrologica Sinica 32, 3441–3455 (in Chinese with English abstract).

Jørgenson, B.B., Isaksen, M.F., Jannasch, H.W., 1992. Bacterial sulfate reduction above 100 °C in deep sea hydrothermal vent sediments. Science 258, 1756–1757.

Kump, L.R., Arthur, M.A., 1999. Interpreting carbon-isotope excursions: carbonates and organic matter. Chemical Geology 161, 181–198.

Leach, D.L., Sangster, D., Kelley, K.D., Large, R.R., Garven, G., Allen, C., Gutzmer, J., Walters, S., 2005. Sediment-hosted lead-zinc deposits: a global perspective. Economic Geology 100th Anniversary, pp. 561–607.

Leach, D.L., Bradley, D.C., Huston, D., Pisarevsky, S.A., Taylor, R.D., Gardoll, S.J., 2010. Sediment-hosted lead-zinc deposits in Earth history. Economic Geology 105, 593–625.

Lepvrier, C., Maluski, H., Tich, V.V., Leyreloup, A., Thi, P.T., Vuong, N.V., 2004. The early Triassic Indosinian orogeny in Vietnam (Truong Son Belt and Kontum Massif): implications for the geodynamic evolution of Indochina. Tectonophysics 393, 87–118.

Lepvrier, C., Vuong, N.V., Maluski, H., Thi, P.T., Tich, V.V., 2008. Indosinian tectonics in Vietnam. Comptes Rendus Geoscience 340, 94–111.

Li, X.B., Huang, Z.L., Li, W.B., Zhang, Z.L., Yan, Z.F., 2006. Sulfur isotopic compositions of the Huize super-large Pb-Zn deposit, Yunnan Province, China: implications for the source of sulfur in the ore-forming fluids. Journal of Geochemical Exploration 89, 227–230.

Li, W.B., Huang, Z.L., Yin, M.D., 2007. Dating of the giant Huize Zn-Pb ore field of Yunnan province, southwest China: constraints from the Sm-Nd system in hydrothermal calcite. Resource Geology 57, 90–97.

Li, B., Zhou, J.X., Huang, Z.L., Yan, Z.F., Bao, G.P., Sun, H.R., 2015. Geological, rare earth elemental and isotopic constraints on the origin of the Banbanqiao Zn-Pb deposit, southwest China. Journal of Asian Earth Sciences 111, 100–112.

Li, B., Zhou, J., Li, Y., Chen, A., Wang, R., 2016. Geology and isotope geochemistry of the Yinchanggou-Qiluogou Pb-Zn deposit, Sichuan Province, Southwest China. Acta Geologica Sinica (English Edition) 90, 1768–1779.

Lin, Z.Y., Wang, D.H., Zhang, C.Q., 2010. Rb-Sr isotopic age of sphalerite from the Paoma lead-zinc deposit in Sichuan Province and its implications. Geology of China 37 488–196 (in Chinese with English abstract).

Liu, H.C., Lin, W.D., 1999. Study on the Law of Pb-Zn-Ag Ore Deposit in Northeast Yunnan, China. Yunnan University Press, Kunming, pp. 1–468 (in Chinese).

Liu, W.H., Zhang, J., Wang, J., 2017. Sulfur isotope analysis of carbonate-hosted Zn-Pb deposits in northwestern Guizhou Province, Southwest China: implications for the source of reduced sulfur. Journal of Geochemical Exploration 181, 31–44.

Lu, Y.H., Han, R.S., Ren, T., Qiu, W.L., Rang, H., Gao, Y., 2015. Ore-controlling characteristics of fault structures and their relations to mineralization at Fulechang Zn-Pb mining district in deposit concentration district of northeastern Yunnan, China. Geoscience 29, 563–575.

Machel, H.G., Krouse, H.R., Sassen, R., 1995. Products and distinguishing criteria of bacterial and thermo-chemical sulfate reduction. Applied Geochemistry 10, 373–389.

Mao, J.W., Zhou, Z.H., Feng, C.Y., Wang, Y.T., Zhang, C.Q., Peng, H.J., Miao, Y., 2012. A preliminary study of the Triassic large-scale mineralization in China and its geodynamic setting. Geology of China 39, 1437–1471 (in Chinese with English abstract).

Muchez, P., Heijlen, W., Banks, D., Blundell, D., Boni, M., Grandia, F., 2005. Extensional tectonics and the timing and formation of basin-hosted deposits in Europe. Ore Geology Reviews 27, 241–267.

Nishizawa, M., Maruyama, S., Urabe, T., Takahata, N., Sano, Y., 2010. Micro-scale (1.5 μm) sulphur isotope analysis of contemporary and early Archean pyrite. Rapid Communications in Mass Spectrometry 24, 1397–1404.

Ohmoto, H., 1972. Systematics of sulfur and carbon isotopes in hydrothermal ore deposits. Economic Geology 67, 551–579.

Ohmoto, H., Goldhaber, M.B., 1997. Sulfur and carbon isotopes. In: Barnes, H.L. (Ed.), Geochemistry of Hydrothermal Ore Deposits, 3rd edition Wiley, New York, pp. 517–611.

Ohmoto, H., Kaiser, C.J., Geer, K.A., 1990. Systematic of sulfur isotopes in recent marine sediments and ancient sediment-hosted base metal deposits. In: Herbert, H.K., Ho, S.E. (Eds.), Stable Isotopes and Fluid Processes in Mineralisation. Geol Dep Univ Extens 23. University of Western Australia, pp. 70–120.

O'Neil, J.R., Clayton, R.N., Mayeda, T.K., 1969. Oxygen isotope fractionation in divalent metal carbonates. Journal of Chemical Physics 51, 5547–5558.

Pass, H.E., Cookem, D.R., Davidson, G., Maas, R., Dipple, G., Rees, C., Ferreira, L., Taylor, C., Deyell, C.L., 2014. Isotope geochemistry of the northeast zone, Mount Polley alkalic Cu-Au-Ag porphyry deposit, British Columbia: a case for carbonate assimilation. Economic Geology 109, 859–890.

Pirajno, F., 2000. Ore Deposits and Mantle Plumes. Springer, Science & Business Media: pp. 1–572 https://doi.org/10.1007/978-94-017-2502-6.

Pirajno, F., 2013. Large igneous provinces (Xiong'er, Dashigou, 827 Ma Event, Tarim, Emeishan) and the Yanshanian tectono-thermal event of eastern China. The Geology and Tectonic Settings of China's Mineral Deposits. Springer, Netherlands, pp. 547–638.

Pullen, A., Kapp, P., Gehrels, G.E., Vervoort, J.D., Lin, D., 2008. Triassic continental subduction in central Tibet and Mediterranean-style closer of the Paleo-Tethys Ocean. Geology 36, 351–354.

Qiu, L., Tang, S.L., Wang, Q., Yang, W.X., Tang, X.L., Wang, J.B., 2016. Mesozoic geology of southwestern China: Indosinian foreland overthrusting and subsequent deformation. Journal of Asian Earth Sciences 122, 91–105.

Reid, A., Wilson, C.J.L., Shun, L., Pearson, N., Belousova, E., 2007. Mesozoic plutons of the Yidun Arc, SW China: U-Pb geochronology and Hf isotopic signature. Ore Geology Reviews 31, 88–106.

Seal, I.R., 2006. Sulfur isotope geochemistry of sulfide minerals. Review of Mineralogy and Geochemistry 61, 633–677.

Shellnutt, J.G., 2014. The Emeishan large igneous province: a synthesis. Geoscience Frontiers 5, 369–394.

Shellnutt, J.G., Denyszyn, S.W., Mundil, R., 2012. Precise age determination of mafic and felsic intrusive rocks from the Permian Emeishan large igneous province (SW China). Gondwana Research 22, 118–126.

Si, R.J., Gu, X.X., Pang, X.C., Fu, S.H., Li, F.Y., Zhang, M., Li, Y.H., Li, X.Y., Li, J., 2006. Geochemical character of dispersed elements in sphalerite from Fule Pb-Zn polymetal deposit, Yunnan province. Journal of Mineralogy and Petrology 26, 75–80 (in Chinese with English abstract).

Si, R.J., Gu, X.X., Xiao, C., Yu, H.T., Wang, Z.W., Chen, Y.J., Qiu, N., 2011. Geochemical character of trace elements in sphalerite from Fule Pb-Zn deposit, Yunnan province. Journal of Mineralogy and Petrology 31, 34–40 (in Chinese with English abstract).

Si, R.J., Gu, X.X., Xie, L.X., Zhang, N., 2013. Geological characteristics of the Fule polymetallic deposit in Yunnan province: a Pb-Zn deposit with dispersed elements and unusual enrichment. Geology and Exploration 49, 313–322 (in Chinese with English abstract).

Tan, S.C., Zhou, J.X., Li, B., Zhao, J.X., 2017. In situ Pb and bulk Sr isotope analysis of the Yinchanggou Pb-Zn deposit in Sichuan Province (SW China): constraints on the origin and evolution of hydrothermal fluids. Ore Geology Reviews https://doi.org/10.1016/j.oregeorev.2017.09.012.

Tang, Y.Y., Bi, X.W., Fayek, M., Hu, R.Z., Wu, L.Y., Zou, Z.C., Feng, C.X., Wang, X.S., 2014. Microscale sulfur isotopic compositions of sulfide minerals from the Jinding Zn-Pb deposit, Yunnan Province, Southwest China. Gondwana Research 26, 594–607.

Taylor, H.P., Frechen, J., Degens, E.T., 1967. Oxygen and carbon isotope studies of carbonatites from the Laacher See District, West Germany and the Alnö District, Sweden. Geochimica et Cosmochimica Acta 31, 407–430.

Tran, T.H., Polyakov, G.V., Tran, T.A., Borisenko, A.S., Izokh, A.E., Balykin, P.A., Ngo, T.P., Pham, T.D., 2016. Intraplate magmatism and metallogeny of North Vietnam. Modern Approaches in Solid Earth Sciences. Springer, Dordrecht:pp. 1–381 https://doi.org/10.1007/978-3-319-25235-3.

Veizer, J., Hoefs, J., 1976. The nature of O^{18}/O^{16} and C^{13}/C^{12} secular trends in sedimentary carbonate rocks. Geochimica et Cosmochimica Acta 40, 1387–1395.

Wang, C.M., Deng, J., Carranza, E.J.M., Lei, X.R., 2014. Nature, diversity and temporal-spatial distributions of sediment-hosted Pb-Zn deposit in China. Ore Geology Reviews 56, 327–351.

Warren, J., 2000. Dolomite: occurrence, evolution and economically important associations. Earth Science Reviews 52, 1–81.

Wei, A.Y., Xue, C.D., Xiang, K., Li, J., Liao, C., Akhter, Q.J., 2015. The ore-forming process of the Maoping Pb-Zn deposit, northeastern Yunnan, China: constraints from cathodoluminescence (CL) petrography of hydrothermal dolomite. Ore Geology Reviews 70, 562–577.

Worden, R.H., Smalley, P.C., Oxtoby, N.H., 1995. Gas souring by the thermo chemical sulfate reduction at 140 °C. AAPG Bulletin 79, 854–863.

Xie, J.R., 1963. Introduction of the Chinese Ore Deposits. Scientific Books Publishing House, Beijing, pp. 1–71 (in Chinese).

Xu, Y., Chung, S.L., Jahn, B.M., Wu, G., 2001. Petrologic and geochemical constraints on the petrogenesis of Permian-Triassic Emeishan flood basalts in southwestern China. Lithos 58, 145–168.

Xu, J.F., Suzuki, K., Xu, Y.G., Mei, H.J., Li, J., 2007. Os, Pb, and Nd isotope geochemistry of the Permian Emeishan continental flood basalts: insights into the source of a large igneous province. Geochimica et Cosmochimica Acta 71, 2104–2119.

Xu, Y., Huang, Z., Zhu, D., Luo, T., 2014. Origin of hydrothermal deposits related to the Emeishan magmatism. Ore Geology Reviews 63, 1–8.

Yan, D.P., Zhou, M.F., Song, H.L., Wang, X.W., Malpas, J., 2003. Origin and tectonic significance of a Mesozoic multilayer overthrust system within the Yangtze Block (South China). Tectonophysics 361, 239–254.

Yan, Z.F., Huang, Z.L., Xu, C., Chen, M., Zhang, Z.L., 2007. Signatures of the source for the Emeishan flood basalts in the Ertan area: Pb isotope evidence. Chinese Journal of Geochemistry 26, 207–213.

Ye, L., Cook, N.J., Ciobanu, C.L., Liu, Y.P., Zhang, Q., Liu, T.G., Gao, W., Yang, Y.L., Danyushevsky, L., 2011. Trace and minor elements in sphalerite from base metal deposits in South China: a LA–ICPMS study. Ore Geology Reviews 39, 188–217.

Yuan, H.L., Yin, C., Liu, X., Chen, K.Y., Bao, Z.A., Zong, C.L., Dai, M.N., Lai, S.C., Wang, R., Jiang, S.Y., 2015. High precision in-situ Pb isotopic analysis of sulfide minerals by femtosecond laser ablation multi-collector inductively coupled plasma mass spectrometry. Science China: Earth Sciences 58, 1713–1721.

Zartman, R.E., Doe, B.R., 1981. Plumbotectonics-the model. Tectonophysics 75, 135–162.

Zaw, K., Peters, S.G., Cromie, P., Burrett, C., Hou, Z.Q., 2007. Nature, diversity of deposit types and metallogenic relations of South China. Ore Geology Reviews 31, 3–47.

Zhang, J., Lin, Y., Yang, W., Shen, W., Hao, J., Hu, S., Cao, M., 2014. Improved precision and spatial resolution of sulfur isotope analysis using NanoSIMS. Journal of Analytical Atomic Spectrometry 29, 1934–1943.

Zhang, C., Wu, Y., Hou, L., Mao, J., 2015. Geodynamic setting of mineralization of Mississippi Valley-type deposits in world-class Sichuan-Yunnan-Guizhou Zn-Pb triangle, southwest China: implications from age-dating studies in the past decade and the Sm-Nd age of the Jinshachang deposit. Journal of Asian Earth Sciences 103, 103–114.

Zheng, Y.F., 1990. Carbon-oxygen isotopic covariation in hydrothermal calcite during degassing of CO_2. Mineralium Deposita 25, 246–250.

Zheng, Y.F., Hoefs, J., 1993. Carbon and oxygen isotopic covariations in hydrothermal calcites. Mineralium Deposita 28, 79–89.

Zheng, M.H., Wang, X.C., 1991. Genesis of the Daliangzi Pb-Zn deposit in Sichuan, China. Economic Geology 86, 831–846.

Zhou, C.X., Wei, C.S., Guo, J.Y., 2001. The source of metals in the Qilingchang Pb-Zn deposit, Northeastern Yunnan, China: Pb-Sr isotope constraints. Economic Geology 96, 583–598.

Zhou, M.F., Yan, D.P., Kennedy, A.K., Li, Y.Q., Ding, J., 2002. SHRIMP zircon geochronological and geochemical evidence for Neo-Proterozoic arc-related magmatism along the western margin of the Yangtze Block, South China. Earth and Planetary Science Letters 196, 1–67.

Zhou, J., Huang, Z., Zhou, G., Li, X., Ding, W., Bao, G., 2011. Trace elements and rare earth elements of sulfide minerals in the Tianqiao Pb-Zn ore deposit, Guizhou Province, China. Acta Geologica Sinica (English Edition) 85, 189–199.

Zhou, J., Huang, Z., Zhou, M., Li, X., Jin, Z., 2013a. Constraints of C-O-S-Pb isotope compositions and Rb-Sr isotopic age on the origin of the Tianqiao carbonate-hosted Pb-Zn deposit, SW China. Ore Geology Reviews 53, 77–92.

Zhou, J., Huang, Z., Yan, Z., 2013b. The origin of the Maozu carbonate-hosted Pb-Zn deposit, southwest China: constrained by C-O-S-Pb isotopic compositions and Sm-Nd isotopic age. Journal of Asian Earth Sciences 73, 39–47.

Zhou, J., Huang, Z., Bao, G., Gao, J., 2013c. Sources and thermo-chemical sulfate reduction for reduced sulfur in the hydrothermal fluids, southeastern SYG Pb-Zn metallogenic province, SW China. Journal of Earth Science 24, 759–771.

Zhou, J.X., Huang, Z.L., Zhou, M.F., Zhu, X.K., Muchez, P., 2014a. Zinc, sulfur and lead isotopic variations in carbonate-hosted Pb-Zn sulfide deposits, southwest China. Ore Geology Reviews 58, 41–54.

Zhou, J.X., Huang, Z.L., Lv, Z.C., Zhu, X.K., Gao, J.G., Mirnejad, H., 2014b. Geology, isotope geochemistry and ore genesis of the Shanshulin carbonate-hosted Pb-Zn deposit, southwest China. Ore Geology Reviews 63, 209–225.

Zhou, J.X., Bai, J.H., Huang, Z.L., Zhu, D., Yan, Z.F., Lv, Z.C., 2015. Geology, isotope geochemistry and geochronology of the Jinshachang carbonate-hosted Pb-Zn deposit, southwest China. Journal of Asian Earth Sciences 98, 272–284.

Zhou, M.F., Zhao, X.F., Chen, W.T., Li, X.C., Wang, W., Yan, D.Y., Qiu, H.N., 2014. Proterozoic Fe-Cu metallogeny and supercontinental cycles of the southwestern Yangtze Block, southern China and northern Vietnam. Earth Science Reviews 139, 59–82.

Zhou, J.X., Wang, X.C., Wilde, S.A., Luo, K., Huang, Z.L., Wu, T., Jin, Z.G, 2018. New insights into the metallogeny of MVT Zn-Pb deposits: a case study from the Nayongzhi in South China, using field data, fluid compositions, and in situ S-Pb isotopes. American Mineralogist 103. https://doi.org/10.2138/am-2018-6238.

Zhu, B.Q., Hu, Y.G., Zhang, Z.W., Cui, X.J., Mo, D.M., Chen, G.H., Peng, J.H., Sun, Y.G., Liu, D.H., Chang, X.Y., 2007. Geochemistry and geochronology of native copper mineralization related to the Emeishan flood basalts, Yunnan Province, China. Ore Geology Reviews 32, 366–380.

Zhu, C., Wen, H., Zhang, Y., Fan, H., 2016. Cadmium and sulfur isotopic compositions of the Tianbaoshan Zn-Pb-Cd deposit, Sichuan Province, China. Ore Geology Reviews 76, 152–162.

Zhu, C.W., Wen, H.J., Zhang, Y.X., Fu, S.H., Fan, H.F., Cloquet, C., 2017. Cadmium isotope fractionation in the Fule Mississippi Valley-type deposit, Southwest China. Mineralium Deposita 52, 675–686.